J Mater Sci: Mater Electron **(2026) 37:364**

Methoxy-substituted phenylacrylonitrile bearing an *m*-CF_3 group: crystal structure and solvent-dependent excitonic-thermodynamic behavior

Leyla Babali Özen[1], Öner Ekici[2,*], Bayram Gündüz[3], Cem Cüneyt Ersanlı[4], Günseli Turgut Cin[1], and Furkan Özen[5,*]

[1] *Department of Chemistry, Faculty of Science, Akdeniz University, Antalya, Türkiye*
[2] *Department of Pharmacy Services, Durağan Vocational School, Sinop University, Sinop, Türkiye*
[3] *Department of Engineering Basic Sciences, Faculty of Engineering and Natural Sciences, Malatya Turgut Ozal University, Malatya, Türkiye*
[4] *Department of Physics, Faculty of Arts and Science, Sinop University, Sinop, Türkiye*
[5] *Department of Mathematics and Science, Faculty of Education, Akdeniz University, Antalya, Türkiye*

Received: 21 December 2025
Accepted: 2 February 2026
Published online: 11 February 2026

ABSTRACT

The structural, electronic, and optical properties of the D-π-A chromophore 3-(4-methoxyphenyl)-2-(3-(trifluoromethyl)phenyl)acrylonitrile **(MTFMAN)** were comprehensively investigated using a multiscale approach combining single crystal X-ray diffraction, UV–Vis spectroscopy, and Density Functional Theory (DFT), including Time-Dependent DFT (TD-DFT) and explicit solvent cluster modeling. X-ray analysis confirmed that the compound crystallizes in a monoclinic system (space group $P2_1/n$) with a unit cell volume of 1520.4(4) $Å^3$, stabilized by dominant non-covalent interactions, specifically π···π stacking and C–H···F interactions. Optical measurements demonstrated significant solvatochromism; as solvent polarity increased from acetone to DMSO, the absorption maximum shifted from 339 to 344 nm, and the experimental optical band gap decreased from 3.116 to 3.062 eV. TD-DFT calculations confirmed that the dominant Intramolecular Charge Transfer (ICT) is stabilized by the polar DMSO environment. Explicit solvent cluster modeling validated these effects, by identifying a stable C − H···O = S interaction with a stabilization energy of -35.58 kJ/mol. Furthermore, thermodynamic properties (heat capacity, entropy, and enthalpy) were evaluated over a wide temperature range of 100–1000 K, with all data accurately fitting second-order polynomial models ($R^2 > 0.999$). These quantitative results highlight the tunability and thermal stability of **MTFMAN** for solution-processed optoelectronic applications.

Address correspondence to E-mail: oekici@sinop.edu.tr; furkanozen@akdeniz.edu.tr
E-mail Addresses: leyla.babaliozen1@gmail.com; bayram.gunduz@ozal.edu.tr; ccersanli@sinop.edu.tr

https://doi.org/10.1007/s10854-026-16754-7

1 Introduction

Interest in organic semiconductors and π-conjugated materials has increased rapidly in both academic and industrial research [1–3] due to the strong interplay between their π-electronic and geometric structures [4]. In particular, electron-accepting and charge-transporting units combined with moieties such as phenylacrylonitrile [5–8] and triazole [9–12] form donor–π–acceptor (D-π-A) push–pull systems with bipolar character, exhibiting enhanced photophysical properties suitable for photovoltaic applications. The performance of these materials is closely linked to charge-carrier mobility [13]. In LEDs and FETs, carriers are injected from metal or conductive oxide electrodes, whereas in solar cells, charge generation occurs through photon-induced separation at the donor–acceptor interface [14]. Furthermore, efficient charge transport strongly depends on solid-state molecular organization, where well-ordered crystal structures and extended π–π stacking interactions reduce energetic disorder [15].

In this context, improving charge-transport–related factors is of great importance [16], as structural defects in the organic layer, surface topology, dielectric polarity, and interfacial traps directly influence carrier mobility and overall material performance [17]. In particular, the chemical structure of the dielectric surface plays a critical role in modulating carrier mobility. Surface-bound substituent groups can interact with charge carriers, thereby enhancing or degrading device performance. Consequently, rational molecular design, together with controlled solid-state molecular aggregation, is essential for improving carrier mobility and light propagation. Moreover, substituents positioned at different locations within the molecular framework significantly influence electron distribution, ionic bonding, and dipole–dipole interactions [18]. These interactions can modify optical properties such as light absorption and emission by altering intramolecular electron transfer, particularly through changes in the energy gap between the highest occupied and lowest unoccupied molecular orbitals (HOMO–LUMO) [19, 20]. Additionally, surface polarity influences the transfer of charge carriers from the dielectric to the organic semiconductor [21]. Solvent–surface interactions can further modify the structure and properties of the organic layer, with high-polarity solvents either facilitating or hindering carrier transport at the interface [22]. Collectively, these effects play a crucial role in determining carrier mobility and the resulting electronic and optical properties of organic semiconductors by modulating the interactions between aromatic units and the surrounding solvent environment [23–26].

Understanding these effects requires comprehensive thermodynamic characterization to elucidate the structural stability, reactivity, and physicochemical properties of organic molecules under varying conditions. In our previous study, the fundamental optical properties of 4MPAN-TFMP were reported as a function of film thickness [27]. In contrast, to elucidate the effects of subtle structural variations on solid-state packing and optoelectronic performance in D–π–A systems, the present study is not limited to thickness-dependent optical properties of thin films. Instead, it is designed to investigate crystal-level molecular organization, temperature-dependent thermodynamic stability, and solvent-induced electronic effects through a solvent-based approach. Moreover, unlike the 4MPAN-TFMP compound, the present system enabled detailed structural analysis by single-crystal X-ray crystallography. Consequently, this study provides deeper insight into the structure–property relationships governing the optical and electronic behavior of π-conjugated organic semiconductors. Recent advances (2025) highlight that the integration of experimental crystallography with density functional theory is crucial for optimizing the photonic performance of acrylonitrile-based materials [28–30].

In this study, experimental techniques were combined with Density Functional Theory (DFT) calculations at the B3LYP/6-31G(d,p) level using Gaussian 03 to systematically investigate the structural [31–33], thermodynamic, and optoelectronic properties of MTFMAN (Fig. 1). UV–Vis spectroscopy and

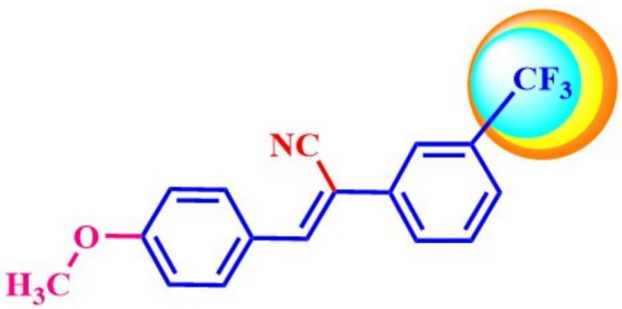

Fig. 1 Molecular structure of the synthesized compound (MTFMAN)

X-ray diffraction were employed to examine its electronic and optical behavior in acetone and dimethyl sulfoxide (DMSO), providing insight into the influence of substitution position on molecular design in π-conjugated organic semiconductors.

Key optical parameters—including refractive index, reflectivity, molar absorption coefficient (ε), mass absorption coefficient (α_mass), optical band gap (E_g), angles of incidence (ϕ_1) and refraction (ϕ_2), and optical contrast (α_c) were analyzed to assess solvent-dependent behavior of MTFMAN. Furthermore, the thermodynamic properties of **MTFMAN**, including heat capacity ($C^0_{p,m}$), entropy (S^0_m), enthalpy (H^0_m), and total energy (E), were calculated over a wide temperature range (100–1000 K) in the gas phase and in the aforementioned solvents (ε_acetone = 20.7; ε_DMSO = 46.7) to assess solvation effects.

Dipole moments and nuclear repulsion energies were also determined to provide insights into solute–solvent interactions and internal molecular cohesion. The temperature-dependent thermodynamic data were fitted using second-order polynomial regression models with high correlation coefficients ($R^2 > 0.999$), confirming the robustness of the fits.

This comprehensive investigation reveals the significant role of solvent polarity and temperature in governing the molecular behavior of **MTFMAN**, offering valuable implications for its potential applications in materials science, pharmaceuticals, and solution-phase chemistry.

2 Experimental and computational methods

2.1 Synthesis of 3-(4-Methoxyphenyl)-2-(3 -(trifluoromethyl)phenyl)acrylonitrile (MTFMAN)

MTFMAN was synthesized via base-catalyzed Knoevenagel condensation procedure, following our previously reported methodology, with slight modifications [8, 28–30]. Complete synthetic and spectroscopic details are provided in the supplementary information (see supplementary). The compound was prepared to to enable a comprehensiveinvestigation of its structural, electronic, and photonic properties, including single-crystal X-ray diffraction analysis.

2.1.1 Crystal growth

Single crystals of **MTFMAN** suitable for X-ray diffraction (XRD) were grown by dissolving the powdered compound in ethanol at room temperature. The resulting solution was heated to reflux under magnetic stirring and then allowed to cool slowly to ambient temperature. The flask was covered with a perforated parafilm layer to facilitate gradual solvent evaporation. After approximately five days under these conditions, well-formed single crystals were obtained.

2.2 Preparation of the MTFMAN solutions

The **MTFMAN** compound was weighed using an AND-GR-200 series analytical balance and subsequently dissolved in ethanol, acetone and DMSO. To ensure homogeneous solutions and optimal experimental conditions, all mixtures were stirred using a vortex mixer. Prior to photophysical measurements, the solutions were filtered through a PTFE filter. Notably, MTFMAN exhibited limited solubility in ethanol and was not completely dissolved in this solvent.

2.3 Characterization and physical measurements

All starting materials and solvents used in the synthesis were obtained from Fluka and Aldrich. Melting points were determined using an electrothermal melting point apparatus. FT-IR spectra were recorded on a Bruker Tensor 27 FT-IR spectrometer with a polystyrene film-calibrated KBr disc. Nuclear magnetic resonance (^{1}H and ^{13}C-APT) spectra were obtained using a BRUKER Spectrospin Avance DPX400 Ultrashield (400 MHz) spectrometer, with tetramethylsilane (TMS) as the internal standard. Optical measurements of the solutions werecarried out using a cylindrical cuvette (Hellma QS-100) with a volume of 3.5 mL and an optical path length of 10 mm, and employing a Shimadzu UV-1800 spectrophotometer at room temperature over a wavelength range of 190–1100 nm.Optical measurements of solutions prepared in ethanol were excluded due to unstable results.

2.4 X-Ray Data collection and refinement processes for MTFMAN

A suitable single crystal of the MTFMAN compound was selected and analyzed using a Bruker APEX-II CCD diffractometer at the Sinop University Scientific and Technological Research Application and Research Center (Sinop University, Türkiye). The single crystal was kept at 296(2) K during data collection. X-ray beams were directed onto the crystals, and the diffracted intensities and angles resulting from atomic scattering were used to generate a three-dimensional electron density map. The crystal structure was solved using the the OLex2-1.5 program by the charge-flipping method and subsequently refined with OLex2-1.5 [34, 35]. The refinement model incorporated 6 restraints and 24 constraints to address partial disorder and to stabilize refinement of the CF_3 group. The following model styles were employed: U_{iso} values for hydrogen atoms were restrained to 1.2 times for C(H) groups; fixed U_{iso} to 1.5 times for methyl C(H,H,H) group C(H,H,H) group. Refinement of riding coordinates: aromatic/amide H groups, C3(H3), C4(H4), C5(H5), C7(H7), C10(H10), C12(H12), C13(H13), C15(H15), C16(H16); idealized Me groups restrained as rotating group, C17(H17A,H17B,H17C) [34]. Disordered distance restraints were applied between disordered fluorine atom positions (F1/F1A, F2/F2A, F3/F3A) bonded to the same carbon atom (C1), all with a sigma value of 0.02 Å.

2.5 Computational procedures

All quantum chemical calculations in this study were performed with the assistance of the Gaussian 03 program package [33]. The molecular geometries were optimized by minimizing the overall energy with respect to all geometrical parameters without applying any symmetry constraints. DFT calculations were performed using the B3LYP exchange–correlation functional [31, 32] and the 6-31G(d,p) basis set, implemented in a computational framework similar to that of the Gaussian 03 software. The selected DFT/B3LYP functional is the most widely adopted hybrid functional in the literature, known for its high accuracy and proven reliability in predicting the optimized geometries, vibrational frequencies, and electronic structures of organic molecules. This approach provides a balanced solution for accurately modeling the critical electronic features in our molecule, such as the conjugated π-system and aromatic rings. The 6-31G(d,p) basis set was chosen as it strikes an ideal balance between computational efficiency and high accuracy. The inclusion of polarization functions (d and p) is crucial for the accurate modeling of electronic charge distribution, especially for polar groups like the acrylonitrile (C≡N) and methoxy ($O-CH_3$) moieties present in MTFMAN. This specific combination forms a solid theoretical foundation for reliable molecular structure analysis, consistent with the experimental X-ray data. GaussView program [36] was used to visualize the optimized molecular structure. The density of states (DOS) and temperature dependent thermodynamic properties in the gas and solution phases were investigated using theoretical calculations.

2.5.1 Computational rigor and reproducibility

Convergence Criterion and Pseudopotential Usage: The energy convergence criterion was set to the most stringent level accepted in the literature for high precision and computational rigor. Given that the molecule consists of lighter elements and the 6-31G(d,p) basis set is an all-electron basis set, no pseudopotentials were utilized in the calculations.

Frequency Scaling Factor: For the comparison between theoretical and experimental vibrational spectra, the standard scaling factor empirically validated in the literature for the B3LYP/6-31G(d,p) methodology was applied [37, 38].

This methodology is further strengthened by the validation of our geometric results against single-crystal XRD data and by our newly included **MTFMAN – $(DMSO)_1$** explicit cluster model analysis (stabilization energy: -35.58 kJ/mol), ensuring the reliability and consistency of our findings.

3 Results and discussion

3.1 Single-crystal X-ray and hirshfeld surface study of MTFMAN: Structural features and lattice stabilization

The molecular structure of **MTFMAN** was determined by single-crystal XRD at 296(2) K using a Bruker APEX-II CCD diffractometer with MoK_α

radiation ($\lambda = 0.71073$ Å). The compound crystallizes in the monoclinic system, space group $P2_1/n$, with unit cell parameters $a = 12.3499(18)$ Å, $b = 6.6311(9)$ Å, $c = 18.640(3)$ Å, $\beta = 95.129(4)°$, and unit cell volume of 1520.4(4) Å^3. The asymmetric unit contains one molecule ($Z = 4$, $\varrho_{calc} = 1.325$ g cm^{-3}). With Olex2 [34], the structure was solved with the olex2.solve [35] structure solution program with Charge Flipping and refined with the olex2.refine [35] refinement package by Gauss–Newton minimisation. The final refinement converged with $R_1 = 0.0521$ and $wR_2 = 0.1161$ for reflections with $I \geq 2\sigma(I)$, demonstrating an excellent fit to the experimental data [36]. The crystallographic parameters and refinement statistics are summarized in Table 1, while additional data, including fractional atomic coordinates, anisotropic displacement parameters, hydrogen atom positions, and geometric parameters, are provided in Supplementary Tables S1–S6. The molecular structure with atom labeling is shown in Fig. 2, and the dataset has been deposited in the Cambridge Crystallographic Data Centre (*CCDC No. 2469549*).

Table 1 Crystal data and structure refinement of MTFMAN

CCDC Deposition number	CCDC 2469549
Identification code	**MTFMAN**
Empirical formula	$C_{17}H_{12}F_3NO$
Formula weight	303.286
Temperature/K	296(2)
Crystal system	monoclinic
Space group	$P2_1/n$
a (Å)	12.3499(18)
b (Å)	6.6311(9)
c (Å)	18.640(3)
α (°)	90
β (°)	95.129(4)
γ (°)	90
Volume (Å^3)	1520.4(4)
Z	4
ρ_{calc} (g cm^{-3})	1.325
μ (mm^{-1})	0.108
F(000)	624.5
Crystal size (mm^3)	0.12 × 0.09 × 0.08
Radiation	Mo K_α ($\lambda = 0.71073$ Å)
2θ range for data collection (°)	4.14 to 52.82
Index ranges	$-15 \leq h \leq 15$, $-8 \leq k \leq 8$, $-23 \leq l \leq 23$
Reflections collected	34,331
Independent reflections	3122 [$R_{int} = 0.0729$, $R_{sigma} = 0.0522$]
Data / restraints / parameters	3122 / 6 / 229
Goodness-of-fit on F^2	1.031
Final R indexes [$I \geq 2\sigma(I)$]	$R_1 = 0.0521$, $wR_2 = 0.1161$
Final R indexes [all data]	$R_1 = 0.1396$, $wR_2 = 0.1482$
Largest diff. peak / hole (e Å^{-3})	0.28 / -0.28

One notable structural feature is the partial disorder observed in the trifluoromethyl (-CF_3) group, in which alternate positions of fluorine atoms (F1/F1A, F2/F2A, F3/F3A) exhibit complementary occupancies [37, 38]. This type of disorder, which is commonly observed in perfluoroaromatic systems, arises from weak van der Waals interactions and rotational flexibility of the CF_3 substituent [39]. The refined atomic displacement parameters (Supplementary Table S2) further indicate a relatively rigid aromatic framework with localized dynamic regions near peripheral substituents such as the CF_3 and methoxy groups [40, 41].

Bond lengths and angles are consistent with expectations for conjugated aromatic-acrylonitrile systems (Supplementary Tables S4-S6). The O1–C14 bond length [1.359(3) Å] is shorter than that of O1–C17 [1.431(3) Å], confirming effective π-conjugation within the methoxy-substituted ring [42]. The N1–C9 distance [1.146(3) Å] corresponds to a strong C≡N triple bond, further confirming conjugation in the acrylonitrile moiety [43]. The dihedral angle between the two phenyl rings is 59.6°, indicating a twisted conformation that restricts π-electron delocalization across the molecule [44].

Planarity deviation analysis reveals that both aromatic rings deviate significantly from coplanarity, as confirmed by high deviation-to-standard deviation (d/s) ratios [45]. Such distortion limits conjugation between donor (methoxyphenyl) and acceptor (trifluoromethylphenyl) moieties, consistent with push–pull electronic characteristics. This torsional arrangement also influences the intermolecular packing by facilitating weak directional interactions in the crystal lattice [46].

Weak intermolecular C–H···N, C–H···F, and π···π interactions contribute significantly to the lattice stabilization. Hirshfeld surface analysis (Fig. 3) highlights red regions near N1 and F2A atoms corresponding to hydrogen bond acceptors, confirming the positions of weak hydrogen bonds [47]. The decomposed 2D fingerprint plots (Fig. 4) quantitatively show the distribution of dominant contacts: F···H/H···F (27.3%), H···H (24.7%), C···H/H···C

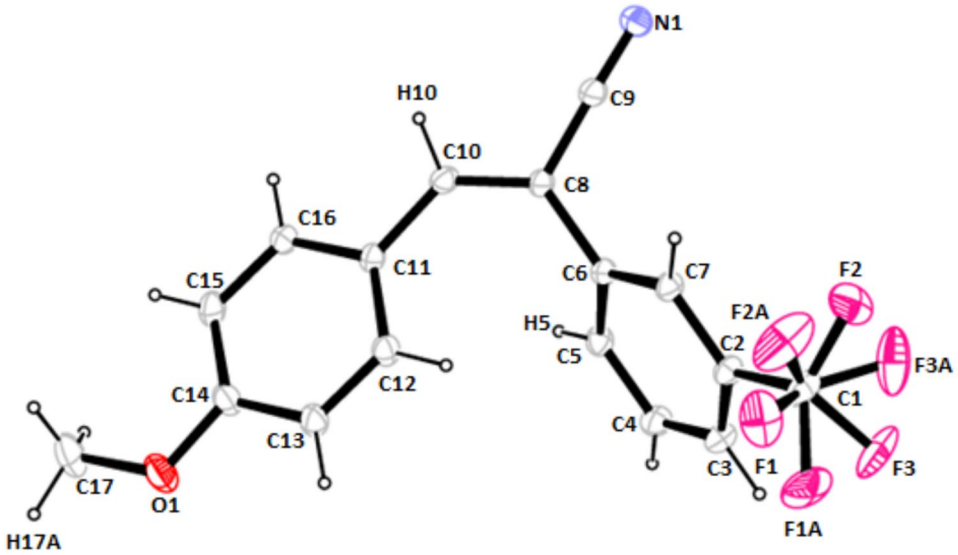

Fig. 2 **MTFMAN** molecular structure, with atom labeling. Displacement ellipsoids are drawn at the 10% probability level

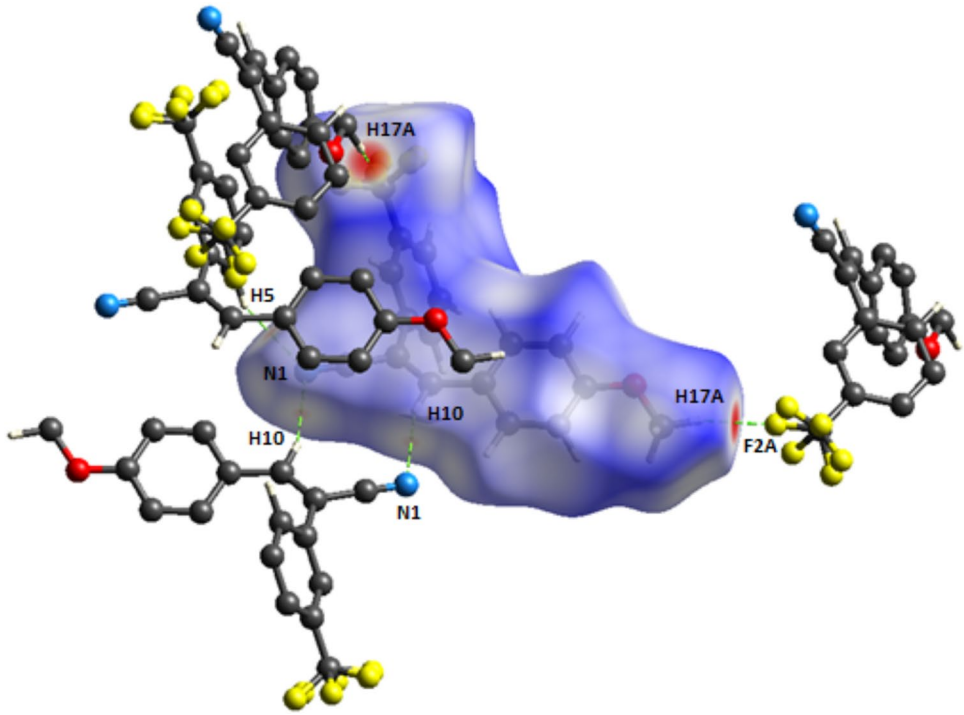

Fig. 3 Hirshfeld surface of **MTFMAN** mapped onto dnorm, with red indication for C-H···N and C–H···F hydrogen bonding interactions [For clarity, all the hydrogen atoms except those involved in intermolecular bonding (H5, H10, and H17A) have been omitted]

(19.1%), and N···H/H···N (12.9%) contribute most to the overall surface. Minor contributions arise from O···H/H···O (4.6%), F···F (3.4%), C···C (2.2%), C···F/F···C (2.2%), C···O/O···C (1.6%), C···N/N···C (1.2%), N···F/F···N (0.6%), and O···F/F···O (0.2%) interactions. These quantitative results confirm that noncovalent forces, though individually weak, collectively stabilize the crystal lattice and maintain structural cohesion [48, 49].

π···π and C–H···π stacking interactions (Supplementary Tables S7 and S8) further contribute to molecular packing [50]. A centroid–centroid distance of 4.95 Å and perpendicular offsets below 3.0 Å indicate weak π···π overlap [51, 52]. The C–H···π contacts, with H···π distances of 2.94 Å, promote directional hydrophobic stabilization and influence the packing arrangement [53].

Overall, the crystallographic investigation confirms that **MTFMAN** exhibits a rigid conjugated backbone with local flexibility in its peripheral substituents. The combined influence of π···π stacking, C–H···N, and C–H···F hydrogen bonds -supported by quantitative Hirshfeld analysis- provides cohesive stabilization for the molecular packing [54–56].

Impact of Intermolecular Interactions on Charge Transport Properties: Beyond lattice stability, these noncovalent interactions have profound implications for the charge transport properties of **MTFMAN**. The π···π stacking facilitates the necessary electronic coupling between π-systems, which is a prerequisite for charge carrier hopping. Simultaneously, the C-H···F interactions function as molecular anchors, reducing the energetic disorder by 'locking' the orientations of the $-CF_3$ and nitrile groups. This structural rigidity is crucial for maintaining consistent hopping pathways and minimizing recombination sites in solid-state devices.

3.2 The optical parameters

3.2.1 *Effects on optical constants of MTFMAN in different solvents*

UV–Vis spectroscopy is an extremely valuable and simple optical technique for studying the optical and electrical properties of organic semiconductor materials. Here, the effect of **MTFMAN** on the optical constants in different solvents, such as DMSO and acetone, was studied using the solvation technique. The research aims to understand how the solvent changes the optical constants of the compound. The polarization properties of the solvent and its interactions with molecules can significantly affect how the compound interacts with light and how it can be used in optoelectronic applications [57, 58]. According to the Beer-Lambert law, there is a direct relationship between the frequency of the light photon and the density of the molecules. As the density increases, so does the light absorption, so that the absorption increases in parallel with the change in the original density of the solution [59].

$$A = \log_{10}(I_0/I) = -\log_{10}(T) = \in CL \quad (1)$$

where I_0 is the intensity of incident monochromatic light on the substance of interest, I is the intensity of monochromatic light leaving the substance, L is the optical path length of light through the cuvette, C is an accurate molar concentration of the absorbing molecule and ε is a molar extinction coefficient or wavelength dependent molar absorptivity of the absorbing molecule.

The absorption spectrum of the **MTFMAN** molecule is presented in Fig. 5. As observed, the absorption curve of the molecule is not clearly visible across all wavelengths in acetone, which may be attributed to the insufficient solubility of the molecule in this solvent. However, distinct absorption maxima are observed for the molecule in both solvents. The absorption peaks appear at 339 nm and 344 nm in acetone and DMSO, respectively. At wavelengths above approximately 400 nm, the absorption becomes minimal and remains nearly constant.

The transmittance spectra of **MTFMAN** solutions in acetone and DMSO are shown in Fig. 6, where the transmittance values are plotted as a function of wavelength. As can be seen, there is a trough around 350 nm for both solvents and the transmittance of the molecule increases sharply from this minimum up to around 400 nm. In addition, the transmittance peak at 270 nm, which was not observed for acetone, appeared in DMSO.

The absorption band edge of the **MTFMAN** molecule was obtained by calculating the first derivative of the optical conductivity. The dT/dλ curve with respect to λ is shown in Fig. 7**.** The absorption band edge values of the molecule for acetone and DMSO solvents were determined as 3.116 and 3.062 eV respectively. This result shows that DMSO solvent is a more ideal choice for optoelectronic devices requiring a lower absorption band edge.

The optical behavior of MTFMAN exhibits a clear solvatochromic effect, characterized by a bathochromic (red) shift as the solvent polarity increases from acetone (λ_{max} = 339 nm) to DMSO (λ_{max} = 344 nm). This shift corresponds to a reduction in the experimental optical band gap from 3.116 eV to 3.062 eV. Such behavior is a signature of the strong intramolecular charge transfer (ICT) within the D–π–A system, where the highly polar DMSO environment (ε = 46.7) provides greater stabilization to the excited state relative to the ground state. This stabilization is further corroborated by our explicit solvent cluster analysis, which identifies a stable C − H···O = S interaction (2.27 Å) specific to the DMSO environment, facilitating enhanced electronic stabilization and the observed reduction in the band gap.

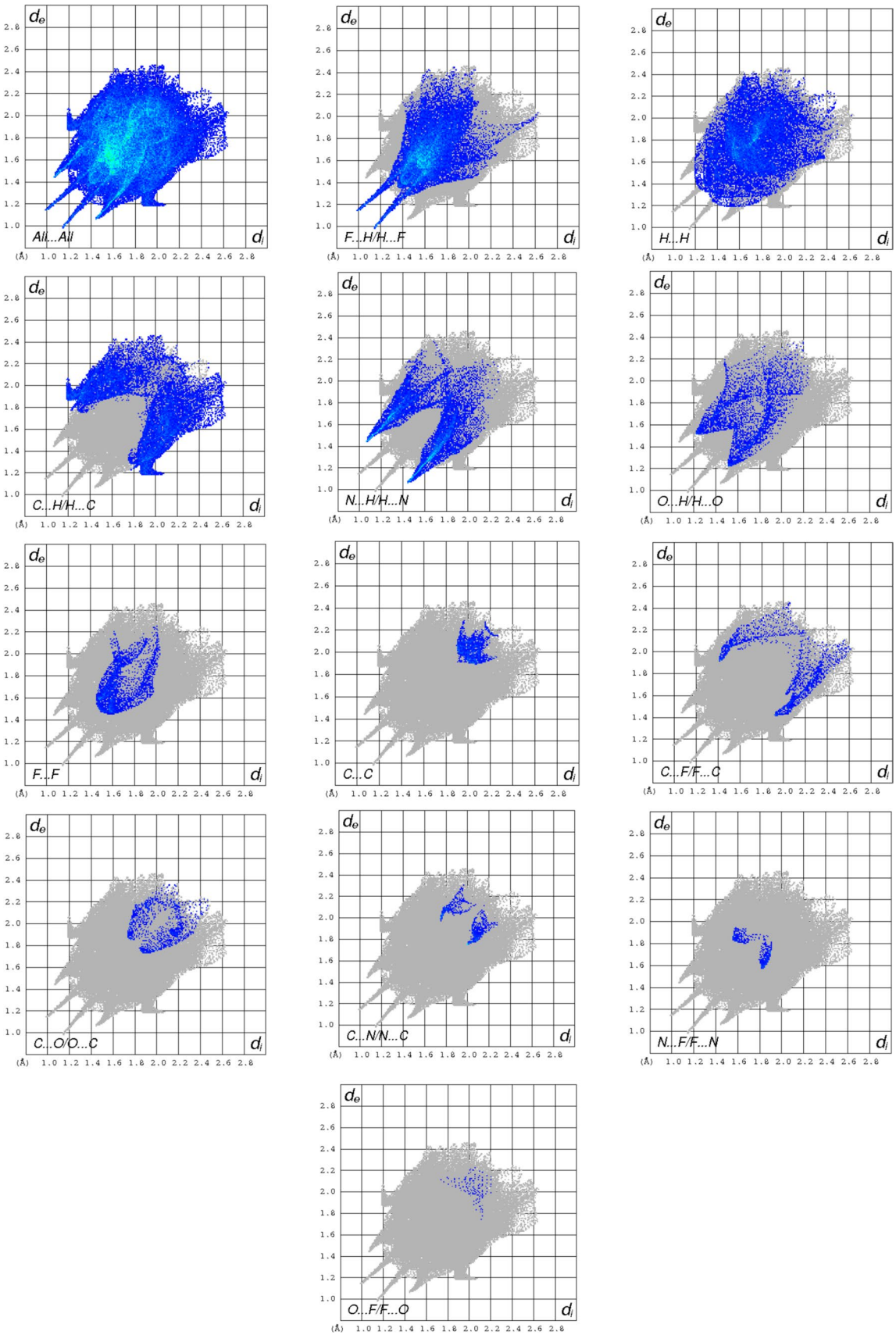
All...All
F...H/H...F
H...H
C...H/H...C
N...H/H...N
O...H/H...O
F...F
C...C
C...F/F...C
C...O/O...C
C...N/N...C
N...F/F...N
O...F/F...O
d_e
d_i
(Å) 1.0 1.2 1.4 1.6 1.8 2.0 2.2 2.4 2.6 2.8

◂**Fig. 4** Decomposed 2D fingerprint plots of observed contacts for **MTFMAN**

To address the request for comparison, the calculated HOMO–LUMO energy gaps ($E_{g,\ calc}$) were compared with the experimental optical band gaps ($E_{g,\ exp}$) derived from the UV–Vis absorption onset (Table 2**)**. In the solution phase, the experimental E_g values are 3.116 eV for Acetone and 3.062 eV for DMSO. The theoretical gaps calculated at the B3LYP/6-31G(d,p) level are 3.739 eV for both solvents. The calculated E_g values are consistently higher than the experimental values, showing deviations of 0.623 eV (Acetone) and 0.677 eV (DMSO). This systematic overestimation of the optical gap is a common and widely documented limitation of the B3LYP functional, particularly when applied to molecules exhibiting strong intramolecular charge-transfer (D − π − A) characteristics. B3LYP functionals often fail to accurately capture the excited-state energy difference due to the inherent lack of long-range correction, which leads to an overestimation compared to the experimentally observed absorption onset. Despite this quantitative deviation, the theoretical calculation successfully reproduces the qualitative trend of solvent effects: the minimal energy difference between the calculated gaps for Acetone and DMSO reflects the stabilizing effect of increasing solvent polarity, which aligns with the experimentally observed 0.054 eV reduction (3.116 eV → 3.062 eV) in the experimental band gap.

To clarify the mechanism responsible for the reduced optical band gap and the potential 'extra absorption' feature observed experimentally in the highly polar DMSO solvent, a detailed TD-DFT analysis was performed (Table 3). The $S_0 \rightarrow S_1$ transition in DMSO is calculated to occur at 359.88 nm with a high oscillator strength ($f = 1.0005$), indicating a highly probable electronic transition. This transition is characterized almost purely by the HOMO → LUMO contribution (99.70%), which confirms the dominant Intramolecular Charge Transfer (ICT) character. This ICT is stabilized by the high-polarity DMSO environment, directly resulting in the experimentally observed lower optical band gap.

Furthermore, the TD-DFT analysis revealed the presence of a second, much weaker transition. The $S_0 \rightarrow S_2$ transition is calculated at 241.63 nm with an excitation energy of 5.1312 eV. This transition is primarily due to the H → L + 3 contribution (72.07%) and exhibits a significantly lower oscillator strength ($f = 0.1000$) compared to the $S_0 \rightarrow S_1$ transition. This secondary, much weaker band suggests an alternate electronic pathway that may correspond to the extra absorption (shoulder or minor peak) feature observed in the UV–Vis spectrum under highly polarizing conditions, thus providing a concrete theoretical explanation.

3.2.2 The thermodynamic analysis at 298.15 K

Thermodynamic properties of compound, computed at 298.15 K by DFT/B3LYP/6-31G(d,p) in Gaussian 03, give cut and dried information regarding the nature of the compound in different environments (Table 4). The gas-phase, in which the molecule is free from solvent interaction, shows maximum values of total thermal energy (169.796 $kcalmol^{-1}$), heat capacity (72.008 $calmol^{-1}K^{-1}$), and entropy (148.868 $calmol^{-1}K^{-1}$). These larger values are attributable to the fact that the molecule has the liberty of free translational, rotational, and vibrational motions [60]. Dipole moment is also at a minimum for the compound when it exists in the gaseous state (3.3472 D) as there is a lack of the polarizing effect of the environment. On the other hand, when they are placed in acetone, a relatively polar aprotic solvent ($\varepsilon = 20.7$), the molecule gets electrostatically stabilized and the net energy comes down to 169.086 $kcalmol^{-1}$ whereas entropy is lowered quite significantly to 143.953 $calmol^{-1}K^{-1}$. Dipole moment also attains the value of 3.9504 D and indicates greater solute–solvent polarization in accordance with the calculation by the continuum models such as the Polarizable Continuum Model (PCM) that introduce dielectric impact on molecular electronic structure [61]. The same, but more significant, effect is seen in DMSO, a highly polar solvent ($\varepsilon = 46.7$), where the total energy goes down to 169.075 $kcalmol^{-1}$, and the dipole moment has a maximum value of 3.9732 D. Although the entropy (144.050 $calmol^{-1}K^{-1}$) and heat capacity (70.102 $calmol^{-1}K^{-1}$) of DMSO is very close to that of acetone, DMSO stabilizes slightly due to its greater dielectric field and ability to polarize the solute more [62].

These entropy and heat capacity reductions on solvents are expressions of restricted molecular motion by solvation, especially in vibrational modes, and agree with thermodynamic theory and solution chemistry experiments [63]. Overall, comparisons across

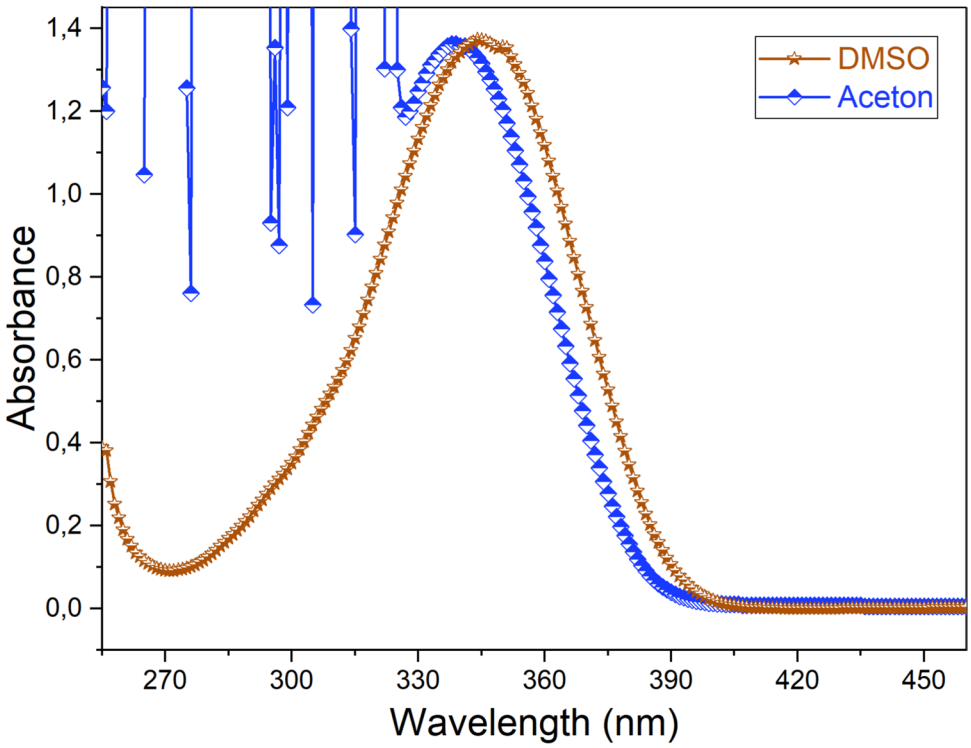

Fig. 5 Absorbance spectra of MTFMAN in acetone and DMSO, illustrating the 5 nm bathochromic shift (λ_{max} = 339 nm to 344 nm) resulting from increased solvent polarity

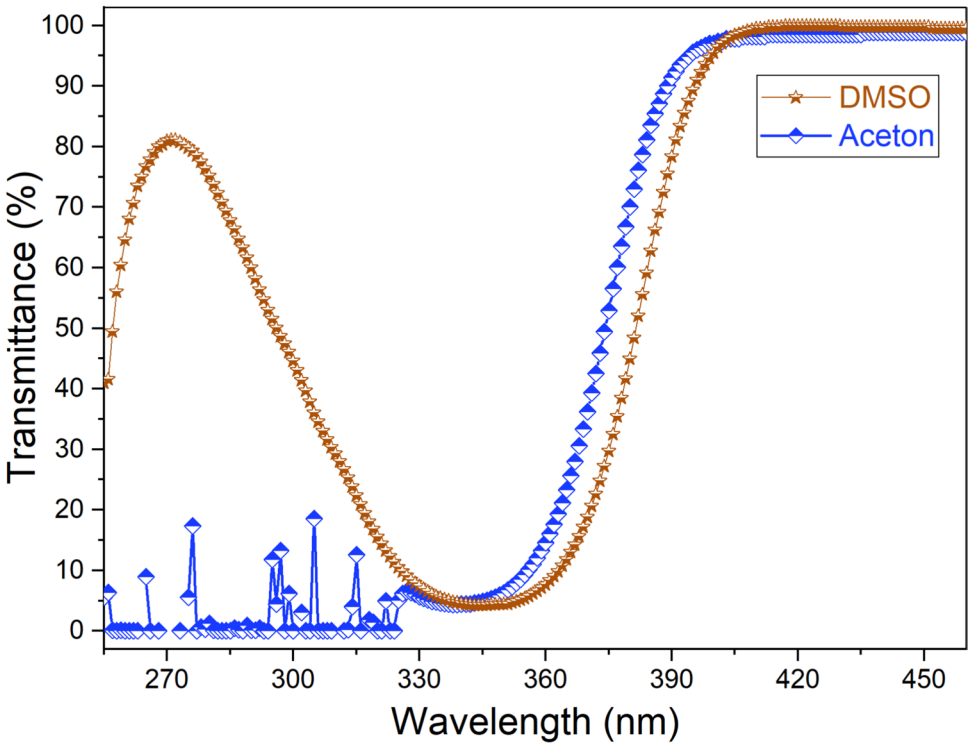

Fig. 6 Transmittance spectra of MTFMAN in acetone and DMSO solutions. The transmittance is plotted as a function of wavelength. Both solvents exhibit a trough near 350 nm, followed by a sharp increase up to ~ 400 nm. A distinct transmittance peak at 270 nm appears in DMSO but is absent in acetone, highlighting solvent-dependent optical behavior

these media show solvent polarity to be a significant variable in molecular property tuning -in this case, improving stability, enhancing dipole moments, and constraining entropy- reflective of the significance of solvation effects in computational and experimental chemical research.

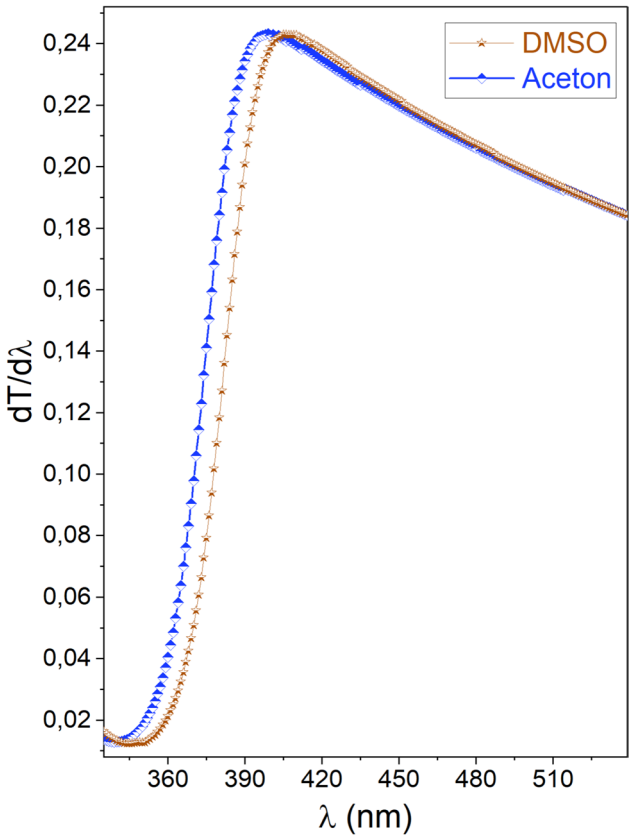

Fig. 7 The first derivative of optical conductivity (dT/dλ) as a function of wavelength, highlighting the solvatochromic impact on the absorption band edge for acetone and DMSO

3.2.3 *Nuclear repulsion energy calculation at 298.15 K*

In compound thermodynamic data, nuclear repulsion energy is provided as 1607.3172540658 Hartree per three environments, *i.e.*, gas phase, acetone, and DMSO (Table 5). The energy is the hard-hitting electrostatic repulsion between the nuclei of atoms within the molecule and a pure geometry-based one. It has no relation with electronic interactions and thus independent of the dielectric constant of the medium or solvation models such as PCM. The nuclear repulsion energy remains uniform across all of the gas phase and media of the solvents, revealing that optimized molecule geometry will essentially be unremarkable regardless of medium it's in solvent. This is no surprise, especially by quite organized organic molecules which contain delocalized π-systems, as where electronic arrangement will be more influenced by solvation than molecular geometry [62]. Although the solvents can affect geometry to a limited degree -especially through hydrogen bonding or strong dipole interactions-, in this case, the effects are negligible or less than the method and basis set used [B3LYP/6-31G(d,p)]. Moreover, in quantum chemical calculations, nuclear repulsion energy is a significant part of the total electronic energy, *i.e.*, nuclear repulsion and electronic interaction terms combined. Since it is independent of solvent model and solvation model, its invariance ensures that solvation plays a very important role in electronic energies and associated thermodynamic properties like dipole moment, total thermal energy, and entropy but not any of the nuclear positions [61].

3.2.4 *Within the range of temperatures 100–1000 K*

Thermodynamic properties of compound were consistently examined in 100–1000 K temperature range according to density functional theory (DFT)

Table 2 Comparison of Calculated and Experimental Optical Band Gaps (E_g) for **MTFMAN**

eV / solvent	DMSO	Acetone	Gas phase
HOMO		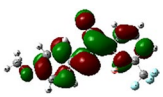	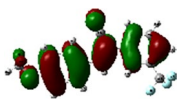
	−5.867	−5.866	−5.894
LUMO	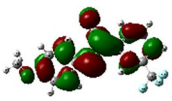		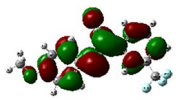
	−2.128	−2.127	−2.125
H–L	3.739	3.739	3.769
$E_{g,\ exp}$	3.062	3.116	–
$E_{g,\ calc} - E_{g,\ exp}$	0.677	0.623	–

Table 3 Experimental and theoretical absorption wavelength, excitation energies E[eV] for **MTFMAN**

Orbital involved in the transitions and major contributions (%)	*E* [eV]	Oscillator strength (*f*)	Theoretical λ_{max} [nm]	Experimental λ_{max} [nm]
Transition singlet-A (Gas Phase)				
H → *L* (99.51)	3.6004	0.8945	344.36 (E.s.: 1)	-
H → *L*+3 (62.31)	5.1841	0.0628	239.16 (E.s.: 7)	
H-2 → L + 2 (22.02)	6.9370	0.4122	178.73 (E.s.: 24)	
Transition singlet-A (Acetone)				
H → *L* (99.69)	3.4583	0.9891	358.51 (E.s.: 1)	339
H → *L*+3 (71.59)	5.1354	0.0963	241.43 (E.s.: 7)	
H-2 → L + 3 (24.00)	6.8675	0.5361	180.54 (E.s.: 23)	
Transition singlet-A (DMSO)				
H → *L* (99.70)	3.4452	1.0005	359.88 (E.s.: 1)	344
H → *L*+3 (72.07)	5.1312	0.1000	241.63 (E.s.: 7)	
H-2 → L + 3 (24.84)	6.8594	0.5430	180.75 (E.s.: 23)	

E.s Excited State, *H* HOMO, *L* LUMO

at B3LYP/6-31G(d,p) level using the Gaussian 03 program, including both gas-phase conditions and also solvent atmospheres like acetone (ε = 20.7) and DMSO (ε = 46.7). The computed parameters-standard molar heat capacity ($C^0_{p,m}$), entropy (S^0_m), enthalpy (H^0_m), and total electronic energy (E)- showed smooth increases with temperature, consistent with rising thermal motion and activation of molecular freedom degrees.

In the gaseous state, these quantities showed very significant increases (*e.g.*, $C^0_{p,m}$ from 30.087 to 154.043 $calmol^{-1}K^{-1}$, S^0_m from 95.098 to 289.459 $calmol^{-1}K^{-1}$, and H^0_m from 2.096 to 99.941 $kcalmol^{-1}$ over the range studied), which indicate significant thermal excitation (Table 6).

On the other hand, slightly lower values were found in both solvent media, with differences between acetone (Table 7) and DMSO (Table 8) being negligible, suggesting that solvation-induced damping of molecular flexibility levels off at a moderate dielectric constant.

Table 4 Comparison of thermodynamic parameters of MTFMAN in gas and solvent phase at 298.15 K

Medium	E($kcalmol^{-1}$)	$C^0_{p,m}$ ($Calmol^{-1}K^{-1}$)	S^0_m ($Calmol^{-1}K^{-1}$)	H^0_m ($kCal\ mol^{-1}$)
DMSO	169.075	70.102	144.050	12.076
Acetone	169.086	70.093	143.953	12.072
Gas-phase	169.796	72.008	148.868	12.592

For instance, at 298.15 K, the $C^0_{p,m}$, S^0_m, H^0_m values for acetone (70.093 $calmol^{-1}K^{-1}$, 143.953 $calmol^{-1}K^{-1}$, and 12.072 $kcalmol^{-1}$, respectively) and DMSO (70.102 $calmol^{-1}K^{-1}$, 144.050 $calmol^{-1}K^{-1}$, and 12.076 $kcalmol^{-1}$) were slightly lower than the values observed in the gas-phase.

These values reflect solute–solvent interactions that restrict conformational degrees of freedom and reduce the number of accessible microstates, with the greatest impact on entropy. Among all parameters, enthalpy was the most temperature-dependent and indicated the sensitivity of the system towards thermal energy input. By and large, the study confirms that while the compound is thermally stable across a broad range of temperatures, its thermodynamic profile is partially influenced by solvent effects, providing crucial data for its performance in chemically rich environments [31, 32].

Fig. 8 illustrates the variation of thermodynamic parameter of compound -standard molar heat capacity ($C^0_{p,m}$), entropy (S^0_m), and enthalpy (H^0_m) –with temperature (100–1000 K) in the gas-phase and in two solvents: acetone and DMSO. The parameters were accurately fitted into second-order polynomial equations with high correlation, as evidenced by the respective correlation coefficients ($R^2 > 0.999$ in both cases). In the gas-phase, the equation for heat capacity has a high temperature dependence, and the enthalpy and entropy equations likewise exhibit high fidelity ($R^2 = 0.99950$ and $R^2 = 0.99996$, respectively), reflecting high predictability over the temperature

Table 5 The electronic and thermodynamic parameters calculated through DFT by employing the basis set of B3LYP/6-31G(d,p) for the compound in the gas phase, as well as acetone and DMSO solvent media, at 298.15 K

Parameters	Medium (Dielectric constant)		
	Gas-phase ($\varepsilon = 1$)	Acetone ($\varepsilon = 20.7$)	DMSO ($\varepsilon = 46.7$)
Energy (k cal mol^{-1})			
Electronic	0.000	0.000	0.000
Translational	0.889	0.889	0.889
Rotational	0.889	0.889	0.889
Vibrational	168.018	167.309	167.298
Total	169.796	169.086	169.075
Zero-point vibrational energy	157.79630	157.60655	157.59193
Nuclear repulsion energy (Hartree's)	1607.3172540658	1607.3172540658	1607.3172540658
Heat capacity [$C^0_{p,m}$ (cal mol^{-1} K^{-1})]			
Electronic	0.000	0.000	0.000
Translational	2.981	2.981	2.981
Rotational	2.981	2.981	2.981
Vibrational	66.046	64.132	64.140
Total	72.008	70.093	70.102
Entropy [S^0_m (cal mol^{-1} K^{-1})]			
Electronic	0.000	0.000	0.000
Translational	43.023	43.023	43.023
Rotational	35.280	35.280	35.280
Vibrational	70.565	65.651	65.747
Total	148.868	143.953	144.050
Rotational constants (GHz)			
A	0.59414	0.59414	0.59414
B	0.10520	0.10520	0.10520
C	0.09195	0.09195	0.09195
Dipole moment (D)	3.3472	3.9504	3.9732

Table 6 Temperature dependence of heat capacity ($C^0_{p,m}$), entropy (S^0_m) and enthalpy (H^0_m) calculated at B3LYP/6-31G(d,p) basis set for the molecule in gas-phase

Medium (Dielectric constant)	Temperature (K)	E(kcalmol^{-1})	$C^0_{p,m}$ (Calmol^{-1} K^{-1})	S^0_m (Calmol^{-1} K^{-1})	H^0_m (kCal mol^{-1})
Gas-phase ($\varepsilon = 1$)	100	159.694	30.087	95.098	2.096
	200	163.750	51.118	123.758	6.352
	298.15	169.796	72.008	148.868	12.592
	400	178.173	92.019	173.478	21.171
	500	188.226	108.477	196.286	31.424
	600	199.761	121.727	217.642	43.157
	700	212.484	132.361	237.540	56.079
	800	226.167	140.997	256.063	69.960
	900	240.633	148.111	273.328	84.625
	1000	255.750	154.043	289.459	99.941

range. Similarly, in acetone and DMSO, the quadratic heat capacity and enthalpy coefficients are closely related to each other, with minimal solvent influence above a threshold dielectric level ($\varepsilon > 20$). Interestingly, entropy in both solvents is a little lower than in the gas-phase, as expected by the constrained

Table 7 Temperature dependence of heat capacity ($C^0_{p,m}$), entropy (S^0_m) and enthalpy (H^0_m) calculated at B3LYP/6-31G(d,p) basis set for the molecule in acetone

Medium (Dielectric constant)	Temperature (K)	E(kcalmol^{-1})	$C^0_{p,m}$ (Calmol^{-1} K^{-1})	S^0_m (Calmol^{-1} K^{-1})	H^0_m (kCal mol^{-1})
Acetone ($\varepsilon = 20.7$)	100	159.365	28.210	92.279	1.957
	200	163.229	49.186	119.612	6.020
	298.15	169.086	70.093	143.953	12.072
	400	177.269	90.127	168.004	20.458
	500	187.134	106.593	190.391	30.521
	600	198.480	119.838	211.403	42.066
	700	211.014	130.462	231.010	54.799
	800	224.506	139.087	249.278	68.489
	900	238.781	146.190	266.318	82.963
	1000	253.705	152.113	282.245	98.086

Table 8 Temperature dependence of heat capacity ($C^0_{p,m}$), entropy (S^0_m) and enthalpy (H^0_m) calculated at B3LYP/6-31G(d,p) basis set for the molecule in DMSO

Medium (Dielectric constant)	Temperature (K)	E(kcalmol^{-1})	$C^0_{p,m}$ (Calmol^{-1} K^{-1})	S^0_m (Calmol^{-1} K^{-1})	H^0_m (kCal mol^{-1})
DMSO ($\varepsilon = 46.7$)	100	159.352	28.224	92.365	1.959
	200	163.218	49.195	119.705	6.024
	298.15	169.075	70.102	144.050	12.076
	400	177.260	90.136	168.103	20.463
	500	187.125	106.602	190.492	30.527
	600	198.472	119.846	211.506	42.072
	700	211.007	130.470	231.114	54.806
	800	224.499	139.094	249.383	68.497
	900	238.775	146.196	266.423	82.972
	1000	253.699	152.118	282.351	98.095

molecular motion in solvation systems. The nearly-identical R^2 values and the polynomial forms of acetone and DMSO [*e.g.*, $C^0_{p,m} = 2.1419 + 0.26449\ T - 1.1529 \times 10^{-4}\ T^2$ ($R^2 = 0.99963$) for acetone] suggest that the thermal response of the compound is somewhat insensitive to increases in solvent polarity at or near moderate levels. Together, these results verify that quadratic equations provide an excellent fit to the temperature-dependent thermodynamic properties of this compound and demonstrate that solvation reduces heat capacity and entropy responses without significantly affecting temperature-dependent curvature. Such data are essential to the compound's physicochemical stability and performance under various conditions, particularly in pharmaceutical and material science applications [31, 32].

The heat capacity equations, entropy, and enthalpy content correlation with temperature change in gas-phase, acetone and DMSO have been fit in the quadratic equation and respective fitting factors R^2 have been depicted by the following equations, respectively.

Gas-phase ($\varepsilon = 1$)

$$C^0_{p,m} = 4.05506 + 0.26441\ T - 1.15195\ x\ 10^{-4} T^2 \left(R^2 = 0.99964\right)$$

$$S^0_m = 67.0320 + 0.29502\ T - 7.29664\ x\ 10^{-5} T^2 \left(R^2 = 0.99996\right)$$

$$H^0_m = -3,17022 + 0.03541\ T + 6.86995\ x\ 10^{-5} T^2 \left(R^2 = 0.99950\right)$$

Acetone ($\varepsilon = 20.7$)

$$C^0_{p,m} = 2.1419 + 0.26449\ T - 1.1529\ x\ 10^{-4} T^2 \left(R^2 = 0.99963\right)$$

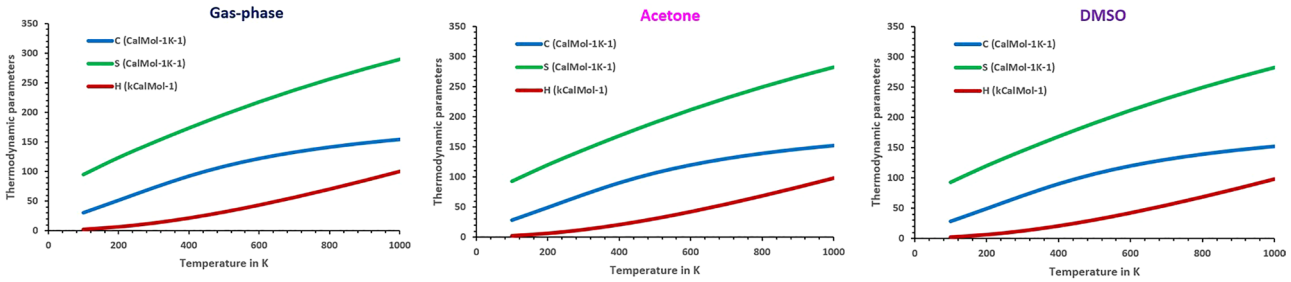

Fig. 8 Plot of calculated thermodynamic parameters *vs.* temperature of the molecule in gas-phase and certain solvents. The solid lines represent second-order polynomial fits ($R^2 > 0.999$) as detailed in Sect. 3.2.4

$$S_m^0 = 64.886 + 0.28490\,T - 6.7761\,x\,10^{-5}T^2 \left(R^2 = 0.99999\right)$$

$$H_m^0 = -3.1214 + 0.03351\,T + 6.8698\,x\,10^{-5}T^2 \left(R^2 = 0.99948\right)$$

DMSO ($\varepsilon = 46.7$)

$$C_{p,m}^0 = 2.15495 + 0.26448\,T - 1.15290\,x\,10^{-4}T^2 \left(R^2 = 0.99963\right)$$

$$S_m^0 = 64.969 + 0.28496\,T - 6.7791\,x\,10^{-5}T^2 \left(R^2 = 0.99999\right)$$

$$H_m^0 = -3.11984 + 0.03352\,T + 6.86970\,x\,10^{-5}T^2 \left(R^2 = 0.99948\right)$$

3.2.5 *Solvation model validation: explicit cluster analysis*

Although the PCM solvation model provides an efficient description of bulk solvent effects, it inherently neglects specific, short-range molecular interactions such as hydrogen bonding. To validate the influence of the PCM model and address this limitation, an explicit solvent cluster model (**MTFMAN – (DMSO)$_1$**) was optimized in the gas phase.

The optimization revealed a stable cluster geometry characterized by a weak C – H···O = S hydrogen bond forming between an aromatic C – H proton of **MTFMAN** and the oxygen atom of DMSO (Fig. 9). This H-bond distance was calculated to be 2.27 Å.

The calculated stabilization energy (ΔE_{stab}) for this complex is – 35.58 kJ/mol. This negative energy confirms the existence of a stabilizing, short-range molecular interaction. Since this specific stabilization energy

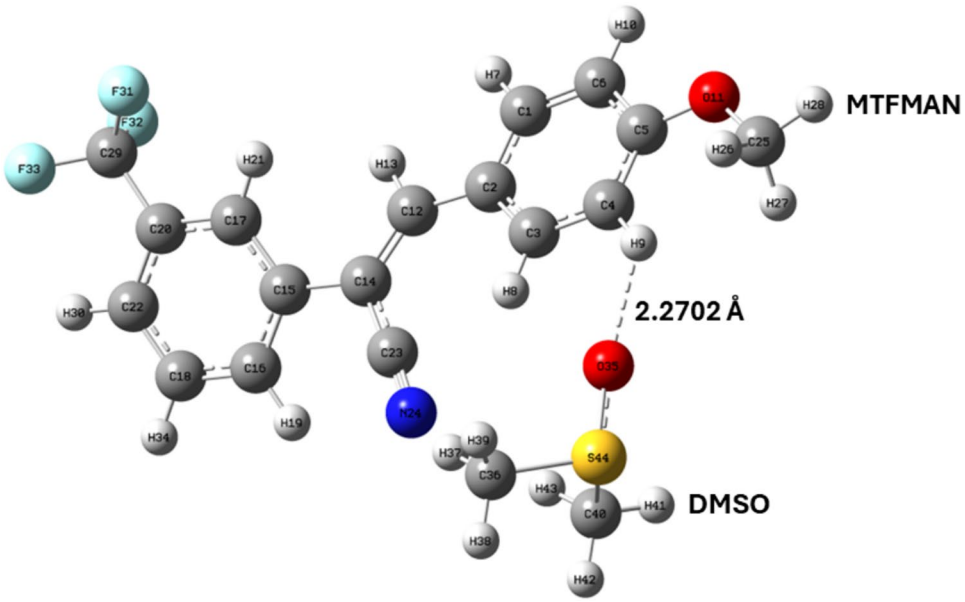

Fig. 9 Optimized geometry of the **MTFMAN – (DMSO)$_1$** explicit solvent cluster model at the B3LYP/6-31G(d,p) level

is not captured by the bulk PCM model, this explicit cluster analysis serves to provide an important quantitative measure of the unique solvent–solute interaction that contributes to the overall stability of **MTFMAN** in the DMSO environment.

3.3 The spectral parameters

The molar extinction coefficient (ε) plays a significant role in determining the electronic transitions of materials. Figure 10a illustrates the molar extinction coefficient curves of the **MTFMAN** molecule as a function of photon energy (E) in acetone and DMSO. As observed, the molar extinction coefficient values of the molecule are on the order of 10^3 L mol^{-1} cm^{-1}. The mass attenuation coefficient (α_{mass}) can be calculated using the following equation [57, 64].

$$\alpha_{mass} = \frac{\varepsilon}{M_A} \tag{2}$$

where M_A, represents the molecular weight of the material. The mass attenuation coefficients of the molecule for acetone and DMSO solvents were calculated using Eq. (2). Figure 10b illustrates the mass attenuation coefficient curves of the molecule as a function of photon energy in acetone and DMSO solvents. The maximum mass attenuation coefficient ($\alpha_{mass\text{-}max}$) values are approximately 3.6 L g^{-1} cm^{-1}.

The optical bandgap (Eg) of organic materials, especially semiconductors, is important for determining their band structures and optical and optoelectronic properties.The optical bandgap values for the molecule in acetone and DMSO can be estimated using the Tauc model (Eq. 3) [65].

$$\alpha = \frac{B\left(h\upsilon - E_g\right)^m}{h\vartheta} \tag{3}$$

where B is the constant, hυ is the photon energy and Eg is the optical band gap of the material. Based on this model, the plot of $(\alpha h\nu)^2$ versus photon energy is shown in Fig. 11. The optical band gap (Eg) of MTFMAN was determined as 3.192 eV in acetone and 3.138 eV in DMSO, revealing a clear narrowing of the band gap with increasing solvent polarity, consistent with a solvatochromic effect. In comparison, the previously studied 4MPAN–TFMP compound exhibited Eg values that varied with film thickness, ranging from 3.223 eV for the thinnest film (7.69 μm) to 3.109 eV for the thickest film (32.45 μm). This contrast highlights that while 4MPAN–TFMP Eg is primarily modulated by film thickness, MTFMAN offers additional tunability via solvent polarity, providing enhanced flexibility for optoelectronic applications.

3.3.1 *Electronic properties and density of states (DOS) analysis*

To theoretically elucidate the electronic properties of the title compound (Fig. 1), Density of States (DOS)

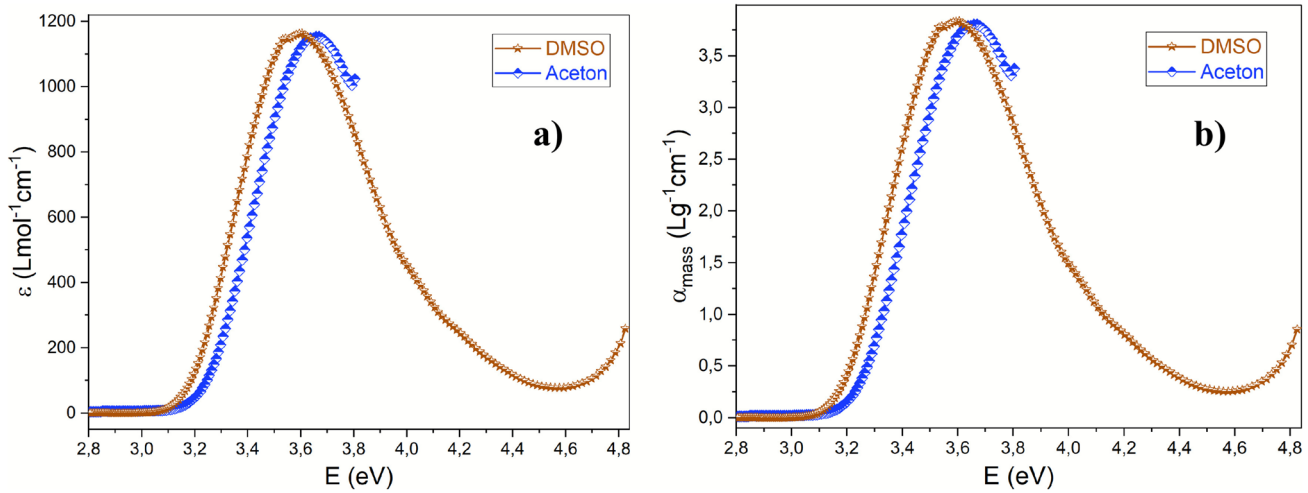

Fig. 10 pectral parameters of MTFMAN in acetone and DMSO solutions. (**a**) Molar extinction coefficient (ε) plotted as a function of photon energy (E), showing values on the order of 10^3L·mol^{-1}·cm^{-1}. (**b**) Mass attenuation coefficient ($\alpha_{mass\text{-}max}$) calculated from ε using Eq. (2), with maximum values around 3.6 L·g^{-1}·cm^{-1}, illustrating solvent-dependent electronic transitions

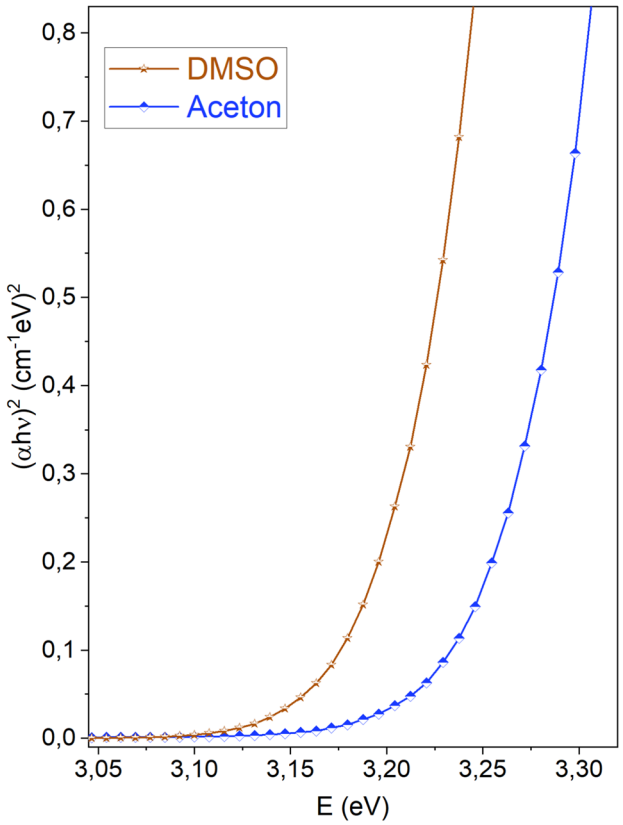

Fig. 11 Tauc plots of $(\alpha h\nu)^2$ versus photon energy (E) for MTF-MAN in acetone and DMSO solutions. The optical band gap (Eg) values were determined as 3.192 eV in acetone and 3.138 eV in DMSO, demonstrating a narrowing of the band gap with increasing solvent polarity (solvatochromic effect)

and Partial Density of States (PDOS) calculations were performed based on Density Functional Theory (DFT). The resulting theoretical DOS plot (Fig. 12) illustrates the contributions of the s and p orbitals from all constituent atoms to the Total Density of States (TDOS). This section provides an interpretation of these results, contextualized by the electronic structure analysis of optoelectronic materials found in the literature [29, 66, 67].

Upon examination of the calculated DOS plot, the valence band (VB), the conduction band (CB), and the forbidden energy gap between them are clearly distinguishable. This observation confirms that the synthesized material exhibits semiconductor characteristics, as anticipated.

3.3.2 *Valence band (VB) analysis*

The valence band, which represents the occupied molecular orbitals of the system, spans the energy region from approximately -0.80 a.u. to the Fermi level (~ -0.25 a.u.). An analysis of the orbital contributions within this region reveals the following:

The s-orbital contributions, represented by the red curve in the plot, are observed to be concentrated in two distinct regions. The first and most significant contribution is located in the deep energy levels between -0.75 a.u. and -0.65 a.u. A second, less intense contribution is observed closer to the Fermi level, within the range of -0.40 a.u. to -0.35 a.u. These s-orbital states in the deep energy levels correspond to the strong sigma (σ) bonds that form the fundamental framework of the molecule. The highly localized nature of these orbitals suggests that their direct contribution to the overall electronic conductivity of the material is limited.

The p-orbitals, represented by the blue curve, play a dominant role across the entire valence band. It is evident that from the -0.60 a.u. energy level up to the Fermi level, the p-orbitals provide a continuous and intense contribution. This finding shows a significant parallel with the p-orbitals of chalcogen atoms (Te-p, S-p) in inorganic semiconductors like Ga_2TeS_2 and Ga_2TeSe_2, which also contribute to both bonding and non-bonding states over a wide energy range as noted in the reference study [67]. In the synthesized organic molecule, this dense p-orbital contribution is strong evidence for the existence of a delocalized π-electron system extending across the aromatic rings and the cyano (-CN) group. These delocalized π-orbitals form the basis of the material's optoelectronic properties and provide the primary pathways for charge carrier mobility.

3.3.3 *Band gap and conduction band (CB) analysis*

A region where the TDOS value approaches zero is present in the plot between approximately -0.25 a.u. (the upper edge of the HOMO) and 0.00 a.u. (the lower edge of the LUMO). This region represents the material's forbidden energy gap (band gap). The existence and width of this gap are the most critical parameters that directly determine the material's electronic and optical properties, such as its absorption and emission wavelengths.

The positive energy region above the Fermi level represents the conduction band, which is composed of unoccupied molecular orbitals. The dominance of p-orbitals (blue curve) continues into this region. The

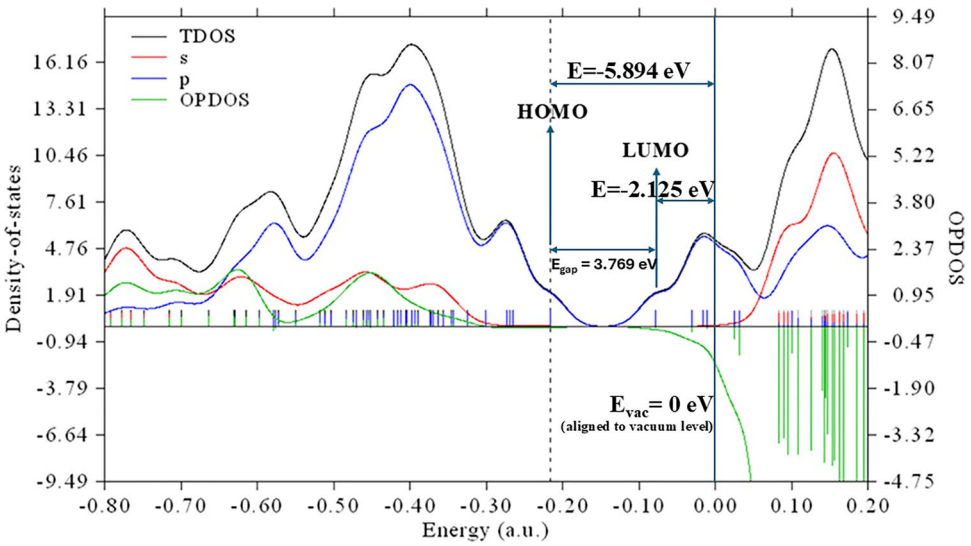

Fig. 12 The Total Density of States (TDOS), s-orbital (red), and p-orbital (blue) Partial Density of States (PDOS) plot for the studied compound

sharp, high-intensity p-orbital peak observed around 0.10 a.u. indicates the presence of low-energy unoccupied states (the LUMO and higher orbitals) where electrons can stably reside upon excitation. This is analogous to the dominant role of Ga-p orbitals in the conduction band of the reference materials and suggests an effective electron-accepting and transporting capability.

3.3.4 Photon energy-dependent optical refraction and contrast behavior in different solvents

The optical fracture property can be explained with the reflection (Φ_1) and refraction (Φ_2) angles of the material. We calculated the Φ_1 [68] and Φ_2 [69] values of the **MTFMAN** Fig. 13 shows the angle of incidence and angle of refraction versus photon energy (E) for acetone and DMSO. The angles of incidence

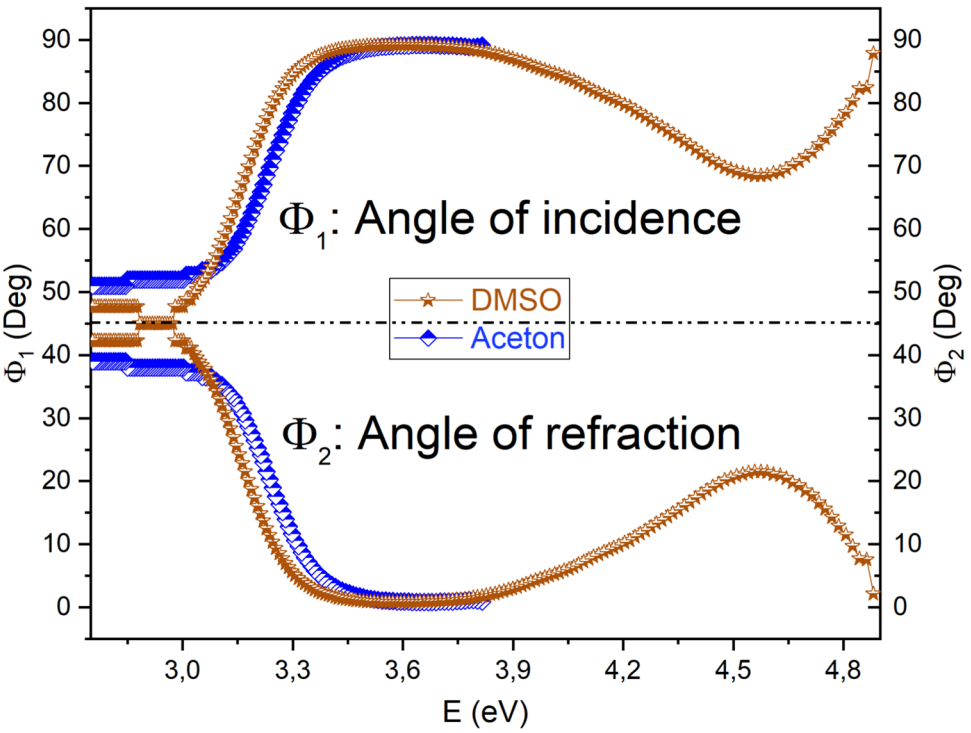

Fig. 13 Photon energy (E) dependence of the reflection (Φ_1, upper panel) and refraction (Φ_2, lower panel) angles of MTFMAN in acetone and DMSO solutions. The angles vary with photon energy and differ from each other, with refraction angles generally lower than incidence angles

and refraction of the molecule vary with wavelength and are different from each other. The upper part of Fig. 13 shows the angle of incidence versus photon energy curves. The angle of incidence of the molecule changed significantly as the photon energy changed. The lower part of Fig. 13 shows the angle of refraction versus photon energy curves for the molecules in acetone and DMSO. The values of the angle of refraction were lower than those of the angles of incidence and changed significantly with varying photon energy. These results provide a more detailed, solvent-sensitive perspective on refractive and contrast dynamics compared to the thickness-dependent optical parameters reported for 4MPAN–TFMP.

Contrast (α_c) is a parameter related to the sensitivity of the material and is an important photophysical parameter. The contrast can be obtained using the following equation [70].

$$\alpha_c = 1 - \left(\frac{n_1}{n_2}\right)^2 \quad (4)$$

The details and results of this equation aid in understanding the photophysical properties of the material. n_1 and n_2 are the refractive indices of the medium and the solution, respectively. The contrast curves of the **MTFMAN** molecule against photon energy for acetone and DMSO solvents are illustrated in Fig. 14. It is observed that the molecule dissolved in DMSO demonstrates sharper and more stable sensitivity with increasing photon energy. Additionally, it is noted that the molecule is light-sensitive and could be utilized in photonic devices. The sensitivity of the molecule dissolved in acetone does not meet the desired level. This result indicates that the material is particularly light-sensitive and can be used in optoelectronic devices. Furthermore, it demonstrates that DMSO is a more ideal solvent for the molecule in terms of its application in fundamental optoelectronic devices.

These solvent-dependent trends complement the refractive and absorption behaviors shown in Figs. 11–13, highlighting that MTFMAN exhibits sharper and more stable contrast in DMSO compared to acetone. This observation underscores the compound's enhanced light-sensitivity in polar solvents, indicating its suitability for optoelectronic and photonic applications.

The refractive index (n), also known as the refractive index coefficient, is a fundamental parameter in optical and optoelectronic applications. n refers to

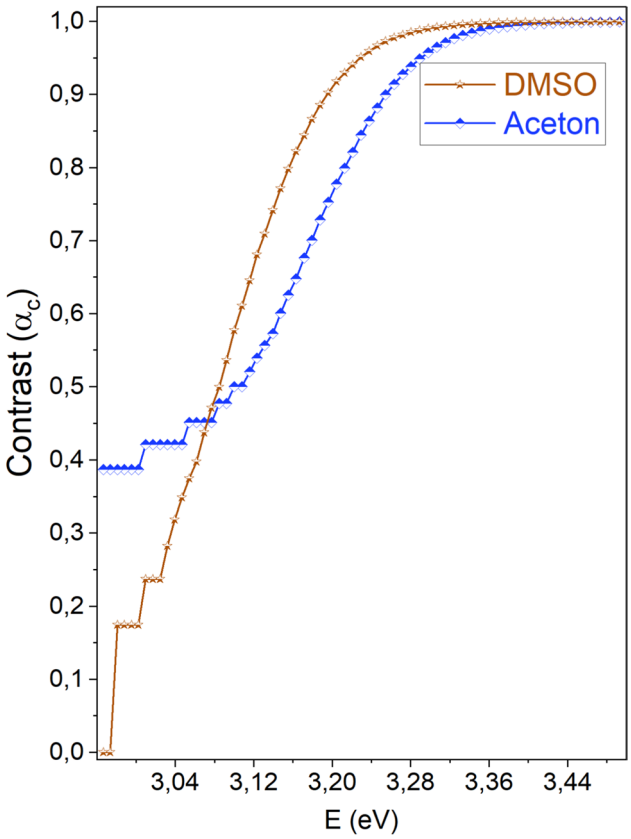

Fig. 14 Optical contrast (α_c) of MTFMAN as a function of photon energy in acetone and DMSO solutions. The compound shows sharper and more stable contrast in DMSO compared to acetone, indicating enhanced light-sensitivity and greater suitability for optoelectronic applications

the speed at which light travels from one medium to another. Materials with high refractive indices have a favourable effect on the transmission and reflection of light. For this reason, the value of the refractive index is calculated using various equations and an attempt is made to obtain the most accurate result. The refractive indices of the MTFMAN molecules were calculated from their optical band gaps using various equations [71], including Reddy, Ravindra, Kumar-Singh, Herve, Vandamme and Moss. The values obtained are shown in Table 9. As can be seen in Table 1, according to the refractive index values obtained, the lowest refractive index values were obtained from the Ravindra relation, while the highest values were obtained from the Reddy relation. In addition, the refractive indices of the **MTFMAN** molecule dissolved in DMSO, calculated from all relations, were higher than those in acetone. The average refractive index values of the **MTFMAN** molecule for acetone and DMSO solvents

Table 9 The absorption band edge (Ee-Abs), optical band gap (Eg), and refractive index values of the MTFMAN molecule calculated using various relations in acetone and DMSO solvents

Solvent	Eg (eV)	E(e-Abs) (eV)	Refractive index values				
			Moss	Ravindra	Herve-Vandamme	Reddy	Kumar and Singh
DMSO	3.062	3.138	2.346	2.138	2.288	2.730	2.329
Acetone	3.116	3.192	2.336	2.105	2.273	2.717	2.316

were 2.349 and 2.366, respectively. These results suggest that DMSO is more ideal for photonic and optoelectronic devices, and materials with high refractive indices (OLEDs, solar cells, sensors, etc.) may exhibit superior performance, opening up new possibilities for the development of more efficient and advanced technologies.

Design Implications for Future Organic Semiconductors: The findings of this work offer significant implications for molecular design. Specifically, the observed sensitivity of the optical band gap to solvent polarity suggests that **MTFMAN**-like structures can be optimized as solvent-tunable sensors. The observed reduction in the optical band gap with increasing solvent polarity is directly relevant to device engineering; such environmental stabilization of the excited state facilitates more efficient exciton dissociation at the donor–acceptor interface, potentially enhancing the quantum efficiency of **MTFMAN**-based organic photovoltaics and OLEDs. Furthermore, the detailed mapping of non-covalent interactions provides a blueprint for using -CF_3 and -OCH_3 substituents to govern solid-state organization in the absence of traditional hydrogen bonding. Future designs should focus on minimizing the torsional angles identified in this study to further enhance π-conjugation and charge carrier mobility.

4 Conclusion

In this study, a comprehensive investigation of the **MTFMAN** chromophore was successfully conducted. Single-crystal X-ray diffraction confirmed that the compound crystallizes in the monoclinic system (space group $P2_1/n$) with a unit cell volume of 1520.4(4) $Å^3$. Peripheral flexibility arises from the dynamic motion of the trifluoromethyl group and the rotational freedom of the methoxy substituent. These features are supported by anisotropic displacement parameters, hydrogen atom refinements, and planarity analysis. Although classical hydrogen-bond donors are absent, the crystal lattice is stabilized by weak intermolecular interactions, including C–H···N, C–H···F, π···π stacking, and C–H···π contacts. Hirshfeld surface analysis confirmed the dominant role of these non-covalent interactions in maintaining structural cohesion.

The second-order polynomial equations ($R^2 > 0.999$) derived fromtemperature-dependent (100–1000 K) thermodynamic data provide a robust predictive tool for determining the material's behavior under operational thermal stress. This characterization is essential for ensuring the long-term physicochemical stability and thermal management of **MTFMAN** in solution-processed optoelectronic applications.

Optical analysis revealed a clear solvatochromic effect; as solvent polarity increased from Acetone to DMSO, the absorption maximum shifted from 339 to 344 nm, respectively. Correspondingly, the experimental optical band gap decreased from 3.116 eV to 3.062 eV, confirming the material's tunability for optoelectronic applications. The average refractive index was determined to be 2.349 in acetone and 2.366 in DMSO, highlighting its potential for efficient light propagation in photonic devices.

While B3LYP/6-31G(d,p) calculations systematically overestimated the optical band gap by approximately 0.65eV, they accurately reproduced the qualitative stabilization trends observed experimentally. Furthermore, explicit solvent cluster analysis quantified a specific C − H···O = S interaction with a stabilization energy of -35.58 kJ/mol, validating the enhanced stability of the molecule in polar DMSO. Overall, the results obtained in the present study complement our previous work by going beyond a mere listing of optical parameters; instead, they elucidate why and how these parameters evolve by correlating crystal structure, thermodynamic models, and quantum–mechanical interactions, thereby establishing a far more comprehensive rational design framework compared to the earlier 4MPAN–TFMP study.

Acknowledgements

We would like to thank the Scientific and Technological Research Council of Türkiye (TÜBİTAK, KBAG-119Z608), Sinop University Scientific and Technological Research Application and Research Center for the use of the Bruker D8 QUEST diffractometer and Akdeniz University Scientific Research Projects Unit (AU-BAP, FBA-2020-5403 and FDK 2022-6056) for their financial support.

Author contribution

Synthesis, Characterization, Methodology, Conceptualization, Writing, L.B.Ö.; Software, Writing–review & editing, Visualization, Validation, Ö.E.; Methodology, Writing–review & editing, Visualization, Supervision, B.G.; Software, Writing–review & editing, Visualization, C.C.E.; Supervision, Writing–review & editing, G.T.C.; Synthesis, Characterization, Methodology, Conceptualization, Writing, Project administration, F.Ö.

Funding

Open access funding provided by the Scientific and Technological Research Council of Türkiye (TÜBİTAK). Scientific and Technological Research Council of Türkiye,TÜBİTAK,KBAG-119Z608,Akdeniz University Scientific Research Projects Unit,AU-BAP,FBA-2020-5403 and FDK 2022-6056

Data availability

Crystallographic data for the structures reported in this article have been deposited at the Cambridge Crystallographic Data Centre, under deposition numbers CCDC 2469549. Copies of the data can be obtained free of charge via https://www.ccdc.cam.ac.uk/structures. All other data supporting the findings of this study are available within the manuscript or from the corresponding author upon reasonable request.

Declarations

Conflict of interest The authors declare no competing interests.

Supplementary Information The online version contains supplementary material available at https://doi.org/10.1007/s10854-026-16754-7.

References

1. M. Kurban, B. Gündüz, F. Göktaş, Experimental and theoretical studies of the structural, electronic and optical properties of BCzVB organic material. Optik **182**, 611–617 (2019). https://doi.org/10.1016/j.ijleo.2019.01.080
2. S. Alam, M.S. Akhtar, E.B. Abdullah, H.S. Kim, S.A. Shin, An effective D-π-A type donor material based on 4-fluorobenzoylacetonitrile core unit for bulk heterojunction organic solar cells. Appl. Sci. **11**(2), 646 (2021). https://doi.org/10.3390/app11020646
3. F. Li, L. Zheng, Y. Sun, S. Li, L. Sun, F. Yang, W. Hu, Cocrystal engineering: towards high-performance near-infrared organic phototransistors based on donor-acceptor charge transfer cocrystals. Sci. China Chem. **66**(1), 266–272 (2023). https://doi.org/10.1007/s11426-022-1450-0

4. O. Ostroverkhova, Organic optoelectronic materials: mechanisms and applications. Chem. Rev. **116**(22), 13279–13412 (2016). https://doi.org/10.1021/acs.chemrev.6b00127
5. R.A. Krishnan, P. Pounraj, R. Govindaraj, M.S. Pandian, P. Ramasamy, Investigating the effect of π-configurations and methoxy substitution on donor and π-spacers based dyes for dye-sensitized solar cell applications–computational approach. Res. Chem. Intermediat. **48**(5), 1877–1906 (2022). https://doi.org/10.1007/s11164-022-04698-6
6. M.J. Percino, M. Cerón, O. Rodríguez, G. Soriano-Moro, M.E. Castro, V.M. Chapela, E. Pérez-Gutiérrez, Conformational and molecular structures of α, β-unsaturated acrylonitrile derivatives: photophysical properties and their frontier orbitals. Molecules **21**(4), 389 (2016). https://doi.org/10.3390/molecules21040389
7. B. Semire, A.K. Oyebamiji, O.A. Odunola, Tailoring of energy levels in (2 Z)-2-cyano-2-[2-[(E)-2-[2-[(E)-2-(p-tolyl) vinyl] thieno [3, 2-b] thiophen-5-yl] vinyl] pyran-4-ylidene] acetic acid derivatives via conjugate bridge and fluorination of acceptor units for effective D–π–A dye-sensitized solar cells: DFT–TDDFT approach. Res. Chem. Intermediat. **43**(3), 1863–1879 (2017). https://doi.org/10.1007/s11164-016-2735-0
8. G. Yakalı, M.B. Çoban, F. Özen, L.B. Özen, B. Gündüz, G.T. Cin, The importance of polymorphism dependent aggregation induced enhanced emission of the acrylonitrile derivative: helical J type and antiparallel h type stacking modes. ChemistrySelect **6**(41), 11392–11406 (2021). https://doi.org/10.1002/slct.202102018
9. J. Salunke, X. Guo, Z. Lin, J.R. Vale, N.R. Candeias, M. Nyman, P. Vivo, Phenothiazine-based hole-transporting materials toward eco-friendly perovskite solar cells. ACS Appl. Energy Mater. **2**(5), 3021–3027 (2019)
10. C.W. Huang, F.C. Chang, Y.L. Chu, C.C. Lai, T.E. Lin, C.Y. Zhu, S.W. Kuo, A solvent-resistant azide-based hole injection/transporting conjugated polymer for fluorescent and phosphorescent light-emitting diodes. J. Mater. Chem. C. **3**(31), 8142–8151 (2015). https://doi.org/10.1039/C5TC01794G
11. A. Abdurahman, A. Obolda, Q. Peng, F. Li, Efficient deep blue fluorescent oleds with ultra-low efficiency roll-off based on 4h-1, 2, 4-triazole cored DA and DAD type emitters. Dyes Pigments **153**, 10–17 (2018). https://doi.org/10.1016/j.dyepig.2018.02.002
12. J. Bauri, R.B. Choudhary, G. Mandal, Recent advances in efficient emissive materials-based OLED applications: a review. J. Mater. Sci. **56**(34), 18837–18866 (2021). https://doi.org/10.1007/s10853-021-06503-y
13. S. Parola, B. Julián-López, L.D. Carlos, C. Sanchez, Optical properties of hybrid organic-inorganic materials and their applications. Adv. Funct. Mater. **26**(36), 6506–6544 (2016). https://doi.org/10.1002/adfm.201602730
14. V. Coropceanu, J. Cornil, D.A. da Silva Filho, Y. Olivier, R. Silbey, J.L. Brédas, Charge transport in organic semiconductors. Chem. Rev. **107**(4), 926–952 (2007)
15. O.D. Jurchescu, J. Baas, T.T. Palstra, Effect of impurities on the mobility of single crystal pentacene. Appl. Phys. Lett. **84**(16), 3061–3063 (2004). https://doi.org/10.1063/1.1704874
16. C. Goldmann, S. Haas, C. Krellner, K.P. Pernstich, D.J. Gundlach, B. Batlogg, Hole mobility in organic single crystals measured by a "flip-crystal" field-effect technique. J. Appl. Phys. **96**(4), 2080–2086 (2004). https://doi.org/10.1063/1.1767292
17. C. Tanase, P.W. Blom, E.J. Meijer, D.M. de Leeuw, Hole transport in polymeric field effect transistors and light-emitting diodes. OFETs II. **5217**, 80–86 (2003). https://doi.org/10.1117/12.507996
18. L. Poulsen, M. Jazdzyk, J.E. Communal, J.C. Sancho-García, A. Mura, G. Bongiovanni, J. Gierschner, Three-dimensional energy transport in highly luminescent host–guest crystals: a quantitative experimental and theoretical study. J. Am. Chem. Soc. **129**(27), 8585–8593 (2007)
19. D. Coskun, B. Gunduz, M.F. Coskun, Synthesis, characterization and significant optoelectronic parameters of 1-(7-methoxy-1-benzofuran-2-yl) substituted chalcone derivatives. J. Mol. Struct. **1178**, 261–267 (2019). https://doi.org/10.1016/j.molstruc.2018.10.043
20. L. Duan, J. Qiao, Y. Sun, Y. Qiu, Strategies to design bipolar small molecules for OLEDs: donor-acceptor structure and non-donor-acceptor structure. Adv. Mater. **23**(9), 1137–1144 (2011). https://doi.org/10.1002/adma.201003816
21. H. Houili, J.D. Picon, L. Zuppiroli, M.N. Bussac, Polarization effects in the channel of an organic field-effect transistor. J. Appl. Phys. **100**(2), 023702 (2006). https://doi.org/10.1063/1.2214363
22. A. Castillo, P. Ceballos, P. Santos, M. Cerón, P. Venkatesan, E. Pérez-Gutiérrez, M.J. Percino, Solution and solid-state photophysical properties of positional isomeric acrylonitrile derivatives with core pyridine and phenyl moieties: experimental and DFT studies. Molecules **26**(6), 1500 (2021). https://doi.org/10.3390/molecules26061500
23. E. Tanış, Optical and photonic properties dependence on HNMB solvents: an emitter molecule for OLEDs. Optik **252**, 168576 (2022). https://doi.org/10.1016/j.ijleo.2022.168576
24. S.E. DeBolt, P.A. Kollman, A theoretical examination of solvatochromism and solute-solvent structuring in simple alkyl carbonyl compounds. Simulations using statistical mechanical free energy perturbation methods. J. Am. Chem. Soc. **112**(21), 7515–7524 (1990)

25. A.H. De Vries, P.T. Van Duijnen, Solvatochromism of the π*← n transition of acetone by combined quantum mechanical-classical mechanical calculations. Int. J. Quantum Chem. **57**(6), 1067–1076 (1996). https://doi.org/10.1002/(SICI)1097-461X(1996)57:6%3c1067::AID-QUA5%3e3.0.CO;2-R
26. V. Manzoni, R. Gester, A.R. da Cunha, T. Andrade-Filho, R. Gester, Solvent effects on Stokes shifts, and NLO response of thieno [3, 4-b] pyrazine: a comprehensive QM/MM investigation. J. Mol. Liq. **335**, 115996 (2021). https://doi.org/10.1016/j.molliq.2021.115996
27. L.B. Özen, F. Özen, B. Gündüz, G.T. Cin, Synthesis and optical properties of 2-(4-trifluoromethylphenyl)-3-(4-methoxyphenyl) acrylonitrile (4MPAN-TFMP) compounds. J. Phys. Chem. Funct. Mater. **7**(2), 208–214 (2024). https://doi.org/10.54565/jphcfum.1583947
28. L.B. Özen, G. Yakalı, M.B. Coban, F. Özen, E. Hür, G.T. Cin, Integration of X-ray crystallography, density functional theory (DFT), and photophysical studies to understand aggregation-induced enhanced emission (AIEE) in dimethoxy acrylonitrile derivatives with donor-acceptor and donor-donor structures. J. Mol. Struct. **1331**, 141451 (2025). https://doi.org/10.1016/j.molstruc.2025.141451
29. L.B. Özen, G. Yakalı, F. Özen, Ö. Ekici, B. Gündüz, G.T. Cin, M. Aygün, Optimizing 3-MeO-BTFMAN thin films: structural insights and photonic performance for advanced optoelectronic applications. J. Mol. Struct. **1333**, 141793 (2025). https://doi.org/10.1016/j.molstruc.2025.141793
30. Ö. Ekici, F. Özen, L.B. Özen, C.C. Ersanlı, B. Gündüz, G.T. Cin, Photophysical insights into TFHA-OP: optimizing optical performance through solvent and film thickness control. Phys. B Condens. Matter **714**, 417524 (2025). https://doi.org/10.1016/j.physb.2025.417524
31. A.D. Becke, Density-functional thermochemistry. III. The role of exact exchange. J. Chem. Phys. **98**, 5648–5652 (1993). https://doi.org/10.1063/1.464913
32. C. Lee, W. Yang, R.G. Parr, Development of the Colle-Salvetti correlation-energy formula into a functional of the electron density. Phys. Rev. B **37**, 785–789 (1988). https://doi.org/10.1103/PhysRevB.37.785
33. M.J. Frisch et al., Gaussian 03, Revision C.02, Gaussian, Inc., 2004.
34. O.V. Dolomanov, L.J. Bourhis, R.J. Gildea, J.A.K. Howard, H. Puschmann, OLEX2: a complete structure solution, refinement and analysis program. J. Appl. Crystallogr. **42**(2), 339–341 (2009). https://doi.org/10.1107/S0021889808042726
35. L.J. Bourhis, O.V. Dolomanov, R.J. Gildea, J.A.K. Howard, H. Puschmann, The anatomy of a comprehensive constrained, restrained refinement program for the modern computing environment-Olex2 dissected. Acta Crystallogr. Sect. A Found. Adv. **71**(1), 59–75 (2015). https://doi.org/10.1107/S2053273314022207
36. R. Dennington, T. Keith, J. Millam, GaussView, Version 4.1.2. [Computer software], Semichem Inc., 2007.
37. A.P. Scott, L. Radom, Harmonic vibrational frequencies: an evaluation of Hartree-Fock, Møller-Plesset, quadratic configuration interaction, density functional theory, and semiempirical scale factors. J. Phys. Chem. **100**(41), 16502–16513 (1996). https://doi.org/10.1021/jp960976r
38. NIST Computational Chemistry Comparison and Benchmark database, NIST Standard Reference Database **101**, Editor: R. D. Johnson III, Release 21 (2002). https://doi.org/10.18434/T47C7Z
39. R.E. Marsh, Some thoughts on choosing the correct space group. Acta Crystallogr. Sect. B Struct. Sci. **51**(5), 897–907 (1995). https://doi.org/10.1107/S0108768195008901
40. V. Petricek, M. Dusek, L. Palatinus, Crystallographic computing system JANA2006: general features. Zeitschrift für Kristallographie-Crystalline Mater. **229**(5), 345–352 (2014). https://doi.org/10.1515/zkri-2014-1737
41. K.N. Trueblood, H.B. Burgi, H. Burzlaff, J.D. Dunitz, C.M. Gramaccioli, H. Schulz, U. Shmueli, S.C. Abrahams, Atomic displacement parameter nomenclature: report of a subcommittee on atomic displacement parameter nomenclature. Acta Crystallogr. Sect. A Found. Crystallogr. **52**(5), 770–781 (1996). (**Acta Crystallographica Section A ISSN 0108-7673.**)
42. G.M. Sheldrick, Crystal structure refinement with SHELXL. Acta Crystallogr. Sect. C Struct. Chem. **71**(1), 3–8 (2015). https://doi.org/10.1107/S2053229614024218
43 F.H. Allen, O. Kennard, D.G. Watson, L. Brammer, A.G. Orpen, R. Taylor, Tables of bond lengths determined by X-ray and neutron diffraction. J. Chem. Soc Perkin Trans. **2**, S1–S19 (1987). https://doi.org/10.1039/P298700000S1
44. A.L. Spek, Single-crystal structure validation with the program PLATON. J. Appl. Crystallogr. **36**, 7–13 (2003). https://doi.org/10.1107/S0021889802022112
45. G.H. Stout, L.H. Jensen, *X-ray structure determination: a practical guide*, 2nd edn. (John Wiley & Sons, New York, Chichester, 1989)
46. D.L. Pavia, G.M. Lampman, G.S. Kriz, J.A. Vyvyan, *Introduction to Spectroscopy* (5th ed.). Cengage Learning. 784, (2014).
47. T. Steiner, G. Koellner, Hydrogen bonds with π-acceptors in proteins: frequencies and role in stabilizing local 3D structures. J. Mol. Biol. **305**(3), 535–557 (2001). https://doi.org/10.1006/jmbi.2000.4301
48. V.R. Thalladi, M. Nüsse, R. Boese, The melting point alternation in α,ω-alkanedicarboxylic acids. J. Am. Chem. Soc.

122(38), 9227–9236 (2000). https://doi.org/10.1021/ja001459

49. J. Zou, D. Zhang, W. Chen, J. Luo, Optimizing the vectorial component of first hyperpolarizabilities of push–pull chromophores to boost the electro-optic activities of poled polymers over broad telecom wavelength bands. Mater. Adv. **2**(7), 2318–2327 (2021). https://doi.org/10.1039/D1MA00086A
50. M. Nardelli, A. Musatti, G. Domiano, G.D. Andreetti, Weighted least-squares planes through the starred atoms. Ric. Sci. **15**(II-A), 807 (1965)
51. G.A. Jeffrey, L. Lewis, Cooperative aspects of hydrogen bonding in carbohydrates. Carbohydr. Res. **60**(1), 179–182 (1978). https://doi.org/10.1016/S0008-6215(00)83475-8
52. R. Taylor, O. Kennard, Crystallographic evidence for the existence of C-H···O, C–H···N, and C–H···Cl hydrogen bonds. J. Am. Chem. Soc. **104**(19), 5063–5070 (1982). https://doi.org/10.1021/ja00383a012
53. A.L. Spek, PLATON SQUEEZE: a tool for the calculation of the disordered solvent contribution to the calculated structure factors. Acta Crystallogr. Sect. C Struct. Chem. **71**(1), 9–18 (2015). https://doi.org/10.1107/S2053229614024929
54. J.K.M. Sanders, C.A. Hunter, The nature of π-π intreactions. J. Am. Chem. Soc. **112**, 5525–5534 (1990). https://doi.org/10.1021/ja00170a016
55 G.A. Jeffrey, W. Saenger, *Hydrogen bonding in biological structures* (Springer, Berlin, 1991)
56. G.R. Desiraju, Hydrogen bridges in crystal engineering: interactions without borders. Acc. Chem. Res. **35**(7), 565–573 (2002). https://doi.org/10.1021/ar010054t
57. B. Gündüz, Effects of molarity and solvents on the optical properties of the solutions of tris [4-(5-dicyanomethylidenemethyl-2-thienyl) phenyl] amine (TDCV-TPA) and structural properties of its film. Opt. Mater. **36**(2), 425–436 (2013). https://doi.org/10.1016/j.optmat.2013.10.005
58. B.T. Aksoy, G. Keşan, E. Özcan, E.T. Eçik, A. Dere, A. Karabulut, B. Çoşut, Solution-processable BODIPY decorated triazine photodiodes and their comprehensive photophysical evaluation. New J. Chem. **44**(5), 2155–2165 (2020). https://doi.org/10.1039/C9NJ05662A
59. A. Beer, Bestimmung der absorption des rothen Lichts in farbigen Flüssigkeiten. Ann. Phys. (Berl.). **162**(5), 78–88 (1852). https://doi.org/10.1002/andp.18521620505
60. D.A. McQuarrie, J.D. Simon, *Molecular thermodynamics* (University Science Books, Sausalito, 1999)
61. J. Tomasi, B. Mennucci, R. Cammi, Quantum mechanical continuum solvation models. Chem. Rev. **105**, 2999–3094 (2005). https://doi.org/10.1021/cr9904009
62 C.J. Cramer, *Essentials of computational chemistry: theories and models*, 2nd edn. (Wiley, 2013)
63. P. Atkins, J. de Paula, Phys. Chem. 9th Edition, W. H. Freeman Co., New York (2010).
64. Y. Li, N. Scales, R.E. Blankenship, R.D. Willows, M. Chen, Extinction coefficient for red-shifted chlorophylls: chlorophyll d and chlorophyll f. Biochimica et Biophysica Acta (BBA) - Bioenergetics **1817**(8), 1292–1298 (2012). https://doi.org/10.1016/j.bbabio.2012.02.026
65. J. Tauc, A. Menth. (1972), States in the gap, *J Non-Cryst Solids* **8–10** ,569–585.O. Stenzel, *The physics of thin film optical spectrum: an introduction*, Springer-Verlag, Berlin Heidelberg, Germany (2005).
66. L.B. Özen, F. Özen, B. Gündüz, G.T. Cin, Ö. Ekici, Experimental and theoretical investigation of the electronic, optical, and structural properties of 2-(3,5-Bistrifluoromethylphenyl)-3-(4-Methoxyphenyl) acrylonitrile for photonic applications. Phys. Status Solidi A **222**, 2400906 (2025). https://doi.org/10.1002/pssa.202400906
67. B. Gul, M.M.A. Al-Hmoud, M.S. Khan, G. Khan, S.M. Aziz, G. Benabdellah, A.M. Binzowaimil, First principle study of the optoelectronic, and thermoelectric properties of novel direct band gap ternary chalcogenides. Physica B **714**, 417528 (2025). https://doi.org/10.1016/j.physb.2025.417528
68. F. Abeles, *Optical properties of solids* (North-Holland Publishing Company Amsterdam, London, 1972)
69 S. Adachi, *Optical constants of crystalline and amorphous semiconductors* (Kluwer Academic Publishers, 1999)
70. B. Gündüz, Investigation of the spectral, optical and surface morphology properties of the N, N′-Dipentyl-3, 4, 9, 10-perylenedicarboximide small molecule for optoelectronic applications. Polym. Adv. Technol. **27**(2), 144–155 (2016). https://doi.org/10.1002/pat.3607
71. S.K. Tripathy, Refractive indices of semiconductors from energy gaps. Opt.Mater. **46**, 240–246 (2015). https://doi.org/10.1016/j.optmat.2015.04.026